Study of ω and ϕ Production via Di-Electron Decay Channel in Proton+Proton Collisions at $\sqrt{s} = 200$ GeV

Kotaro M Kijima (M060291)
Graduate School of Science, Hiroshima University

February 28, 2008

Contents

List of Figures

Chapter 1

Introduction

The all matters constructing "our world" consist of elementary particle, quarks and leptons. For instance, the Hydrogen atom is composed of an electron and a proton. Where the electron is a point particle which is classified into lepton, the proton is known to be a composite particle consisting of three quarks, which are held together by gluons. The state of the nuclear matter is described by the Quantum Chromo-Dynamics(QCD).

	Mass $[MeV/c^2]$	
quark	Bare Quark	Const. Quark
down	3 - 6	$\approx$ 300
up	1.5 - 5	$\approx$ 300
strange	60 - 170	$\approx$ 450
charm	1100 - 1400	
bottom	4100 - 4400	
top	168×10^3 - 179×10^3	

Table 1.1: mass of the quarks:Listed are the mass of "bare" quarks(current quark) which would be measured in the limit $Q^2 \to \infty$ as well as the mass of constituent quarks, i.e., the effective mass of quarks bound in hadrons. [2]

The most of light hadron masses are generated due to the spontaneous breaking of the chiral symmetry. Due to the effect of chiral symmetry restoration, the mass of the hadron, especially light vector mesons(ρ, ω, ϕ), may be shifted and/or modified in the hot matter created by the heavy ion collisions. The study of mass modification is an important topic to understand the mechanism of generation of hadron mass.

Lattice QCD simulations indicate a tendency towards chiral restoration at temperatures $T \sim$150-200 MeV [3]. The density dependence in addition to temperature dependence of the chiral symmetry was calculated. Figure 1.1 shows the schematic behavior of the $< \bar{q}q >$, which is the order parameter of the symmetry, calculated with the Nambu and Jona-Lasinio (NJL) model [4]. According to the calculation, the $< \bar{q}q >$ shows the sudden drop at the critical temperature as expected by lattice calculation (See Figure 1.2). On the other hand, the $< \bar{q}q >$ decreases linearly to the density and the chiral symmetry will restore even at the normal nuclear density.

Hatsuda and Lee calculated the density dependence of the mass of the vector mesons based on QCD sum rules to reach the conclusion that the mass shift is approximately linear to the density in $0 < \rho < 2\rho_0$, and significantly decease for ρ, ω and ϕ at normal density shown in Figure 1.3.

Therefore, low-mass vector mesons are considered the most sensitive probe of chiral symmetry restoration. Over the past few decades, a considerable number of studies have been conducted on mass shift and/or modification. In the next section, we are going to introduce the interesting results reported from CERES/NA45, NA60 and KEK-PS E325.

The Relativistic Heavy Ion Collider (RHIC) is constructed at Brookhaven National Laboratory (BNL) to provide collisions of heavy ion at the center of mass energy ($\sqrt{s_{NN}}$) up to 200GeV and proton at the center of mass energy ($\sqrt{s}$) up to 500GeV. The Pioneering High Energy Nuclear Interaction eXperiment (PHENIX) is one of four experiments in RHIC and specialized experiment for measurement of lepton and photon. The one of the main goal in the PHENIX experiment is to observe the mass shift or modification of low mass vector mesons (ρ, ω, ϕ) in high temperature system created by heavy ion collisions due to the Chiral Symmetry Restoration, in comparison with the result on normal density such as KEK-PS E325 experiment

The study of the light vector mesons in proton+proton collisions is an important baseline for the various heavy ions collisions such as Au+Au, Cu+Cu and d+Au. We, The PHENIX collaboration, recorded the data in proton+proton collisions at $\sqrt{s} = 200$GeV during the year 2005.

The purpose of this work is to find out whether mass shift are observed or not in proton+proton collisions and to provide reference data for baseline of heavy ion collisons. To study ω/ϕ meson production, their di-electron decay channel was used. Unlike hadrons, electrons do not interact strongly with the medium. The measurement of electron pairs from vector meson is therefore a good probe to study chiral symmetry restoration since electrons carry the original information.

In Chapter 2, we will introduce the setup of the PHENIX experiment. In

Chapter 3, we will describe the detailed procedure of this work. In Chapter 4, the result of this work are shown and discussed about it. Chapter 5, we will conclude this work.

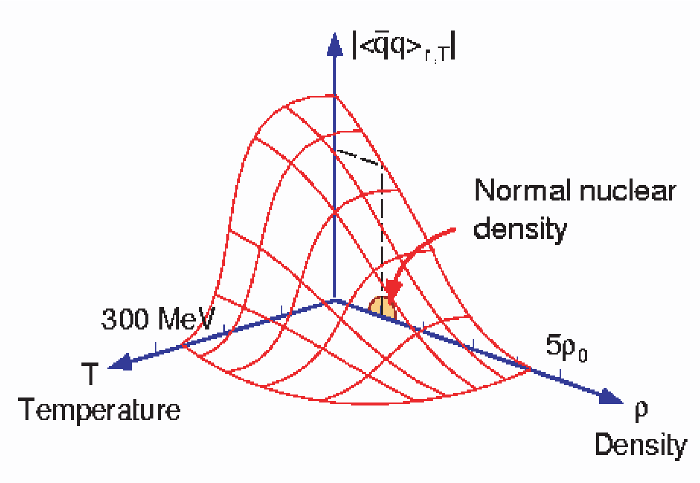

Figure 1.1: Density and temperature dependence of $<\bar{q}q>$ [4]

1.1 Experimental results

1.1.1 CERN-SPS CERES/NA45

The CERES/NA45 experiment [8] measured e^+e^- pair production in central Pb-Au collision 158A GeV at CERN-SPS. A significant excess of the e^+e^- pair yield over the expectation from hadron decay was observed. The date clearly favor a substantial in-medium broadening of the ρ mesons spectral function over a density-dependent shift of the ρ pole mass at SPS energy [9].

1.1.2 CERN-SPS NA60

The NA60 experiment measured low mass muon pair in 158A GeV Indium+Indium collisions at the CERN-SPS. a peaked structure is seen in all cases, broadening strongly with centrality, but remaining essentially centered around the position of the nominal ρ pole. At the same time, the total yield increases relative to the cocktail ρ, their ratio reaching values above 4 for M<0.9 GeV/c^2 in the most central bin [10]. Such values are consistent with the results found by CERES/NA45.

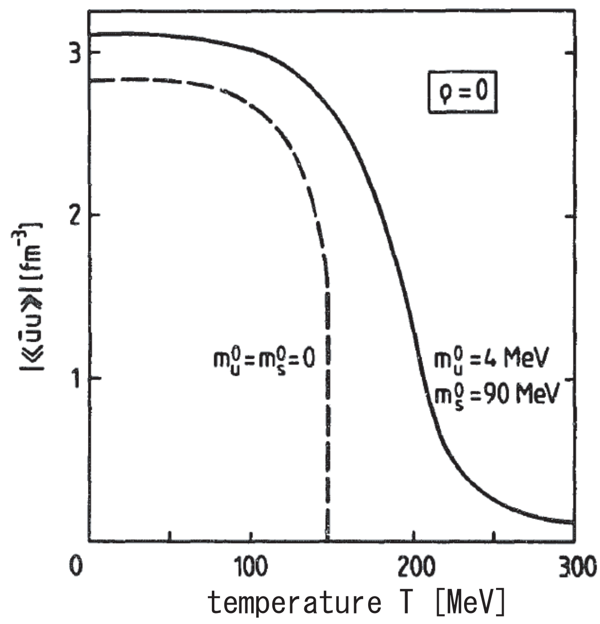

Figure 1.2: The magnitude of the thermal u-quark condensate as a function of temperature, at zero baryon density [4].

1.1.3 KEK-PS E325

The KEK-PS E325 experiment [11] was conducted at the KEK 12-GeV Proton-Synchrotron, in order to search for in-medium mass modification of vector mesons in the reaction 12GeV proton + A $\rightarrow$ ρ, ω, ϕ + X $\rightarrow$ e^+e^- + X'. The data obtained with a copper target revealed a significant excess on the low-mass side of the ϕ meson peak in the $\beta\gamma_\phi < 1.25$ region (See Fig.1.6), Added to this, also the excess on the low-mass side of the ω peak(See Fig.1.7) due to the spectral shape modification of ϕ, ω and ρ mesons, respectively[12][13].

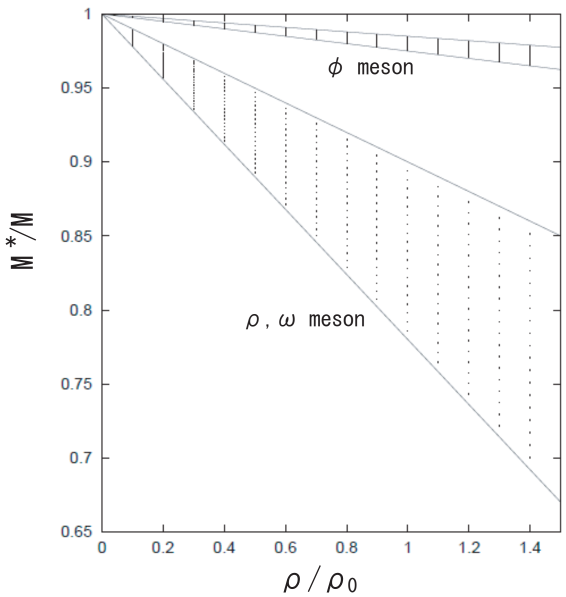

Figure 1.3: Mass of ρ, ω *and* ϕ meson as a function of density [6]

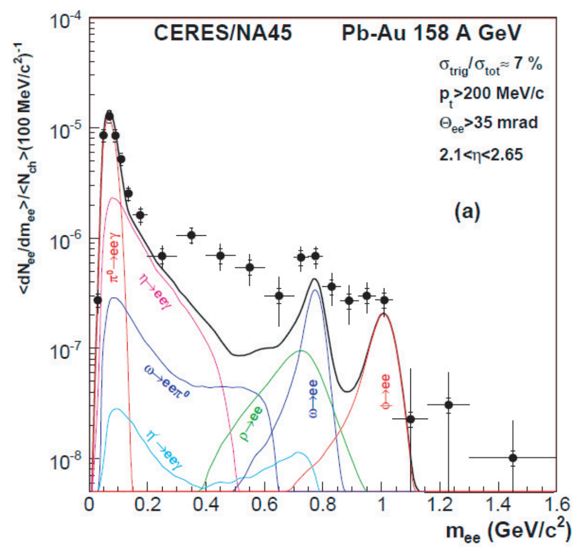

Figure 1.4: Invariant e^+e^- mass spectrum compared to the expectation from hadronic decay at the CERES/NA45 experiment [9]

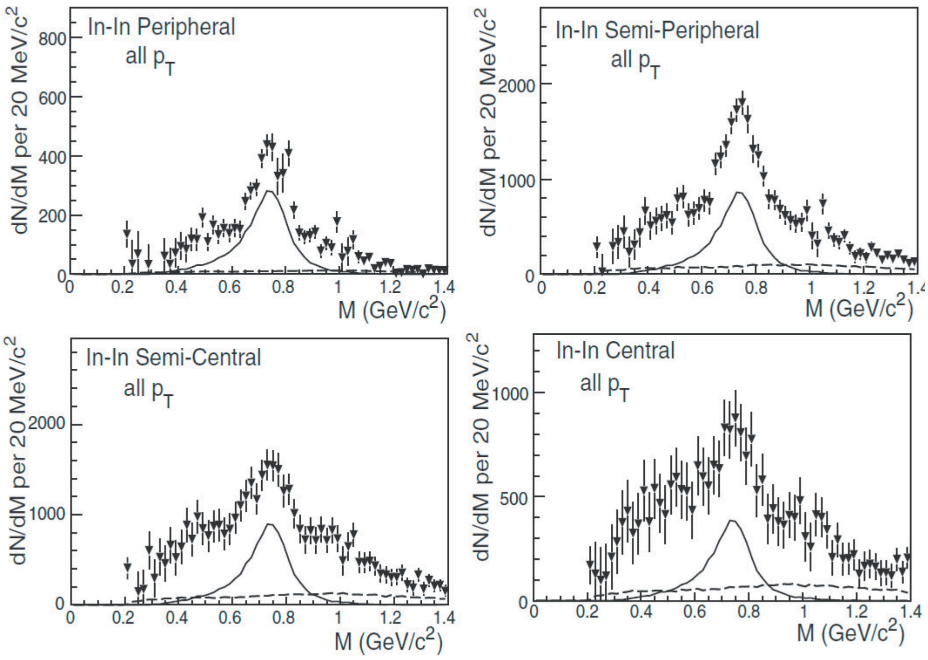

Figure 1.5: Excess mass spectra of $\mu^+\mu^-$ at the NA60 experiment. The known decay $\rho \rightarrow e^-e^+$ (solid line) and the level of uncorrected charm decay (dashed line) are shown comparison. [10]

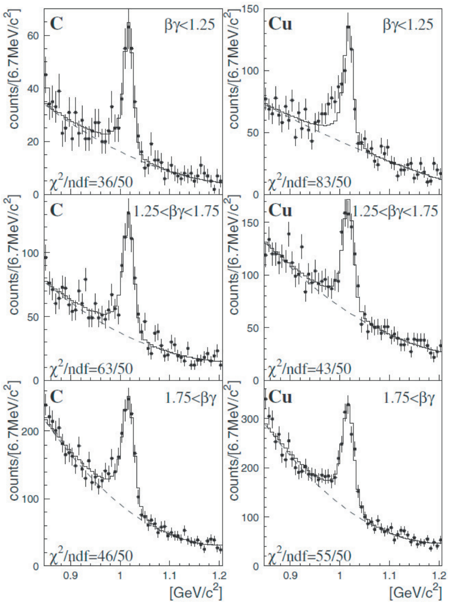

Figure 1.6: Invariant mass spectra of e^+e^- divided into $\beta\gamma$ for the (a)C and (b)Cu target at KEK-PS E325 experiment. The solid lines represent the fit result with an expected $\phi \to e^+e^-$ shape and a quadratic background [12]

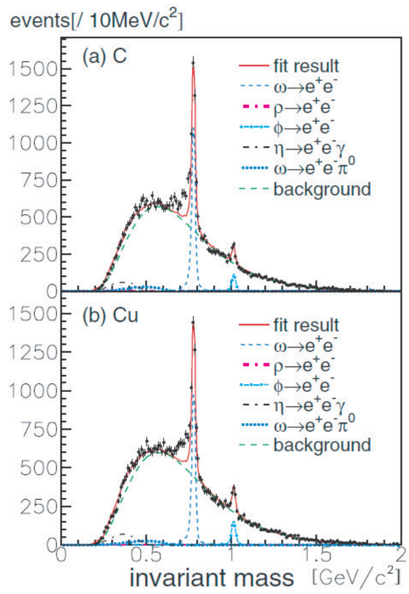

Figure 1.7: Invariant mass spectra of e^+e^- for the (a)C and (b)Cu target at KEK-PS E325 experiment. The solid lines ate the fit result, which is the sum of the known hadronic decays together with the combinatorial background. [13]

Chapter 2

Experimental Setup

The RHIC complex and PHENIX detector are overviewed in this chapter. The description of the RHIC complex is described in Section 2.1, and the PHENIX detecors is described in Section 2.2.

2.1 RHIC

The Relativistic Heavy Ion Collider (RHIC) [14] at Brookhaven National Laboratory (BNL) in the United State was built to study the nuclear physics. The maximum energy at RHIC for heavy ion is 100GeV per uncleon and that for proton is 250GeV. The heavy ion and proton produced at the source are transported through a Tandem Van de Graaff and proton linac, respectively, and accelerate at Booster Synchrotron and the Alternating Gradient Synchrotron (AGS), after that, injected to RHIC. The RHIC ring has a circumference of 3.8km with the maximum bunch of 120 and the designed luminosity is $2 \times 10^{26}\ cm^{-2}\ s^{-2}$ for Au ion and $2 \times 10^{32}\ cm^{-2}\ s^{-2}$ for proton. The RHIC consists of two quasi-circular concentric rings, one("Blue Ring") for clockwise and the other("Yellow Ring) for counter-clockwise. The rings cross at six interaction points. Four experiments, PHENIX, STAR, BRAHMS and PHOBS are build in each one of six interaction points.

The PHENIX, the Pioneering High Energy Nuclear Interaction eXperiment [15], is one of four experiments and specialized experiment for measurement of lepton and photon. In this analysis, the data collected by PHENIX was used. The Detector design is described in the next subsection.

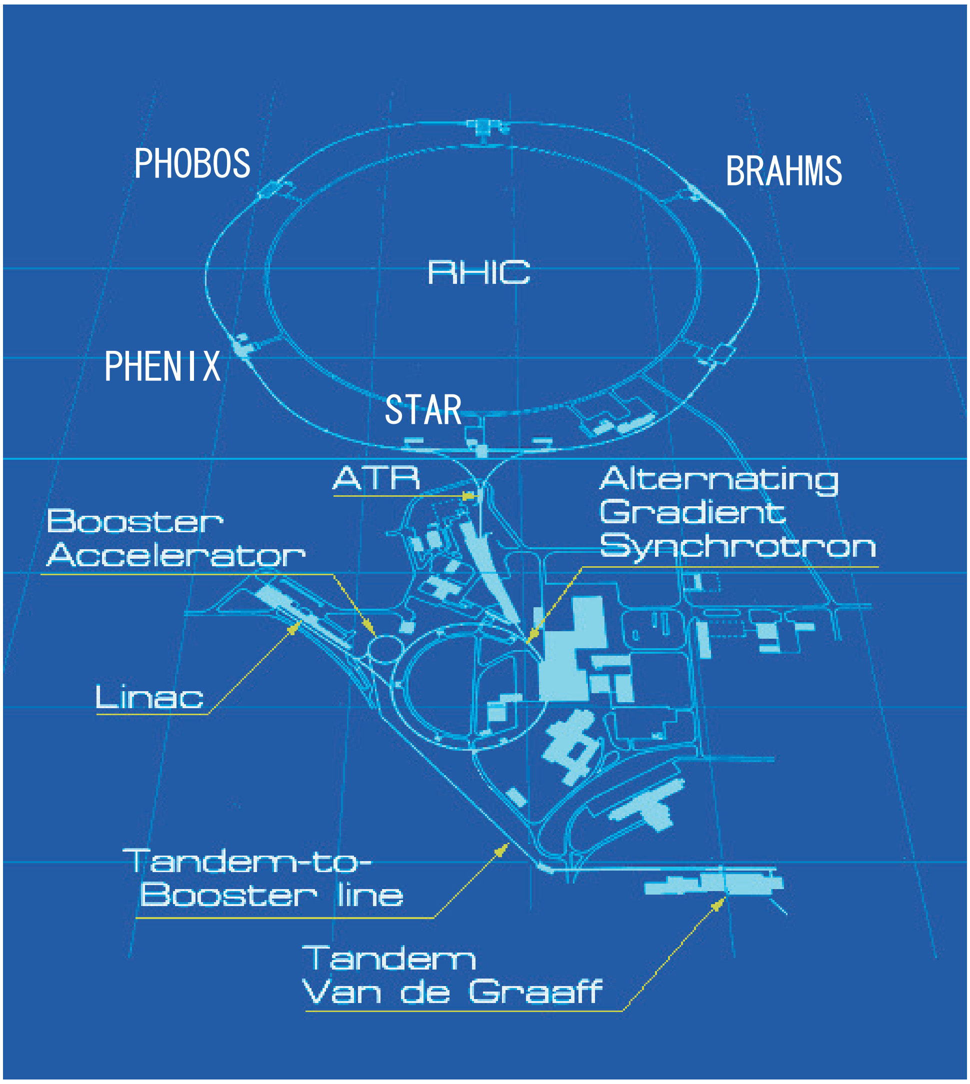

Figure 2.1: RHIC complex

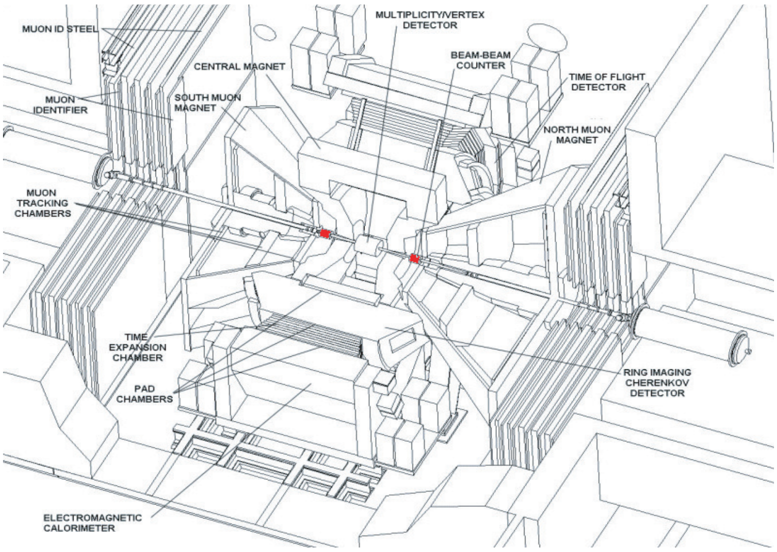

Figure 2.2: overview of The PHENIX Detector

2.2 PHENIX Detector overview

The PHENIX detector consists of 2 central arms [20] [21] [23] which has pseudo-rapidity coverage of ± 3.5 and 180° azimuthal angle in total, 2 muon arms [24] which has pseudo-rapidity coverage of ± (1.2-2.4), and beam detectors [16] which is near the beam pipe.

2.3 Beam Detectors

The main purpose of inner detectors is make triggers and to measure the luminosity and centrality in heavy ion collisions. In this section, mainly BBC and ZDC are discribed.

2.3.1 Beam Beam Counters (BBC)

Beam Beam Counters(BBC) [17] are located on North and South side at 144.35cm along beam pipe from the collision point and covers the pseude-rapidity from 3.0 to 3.9. Each of them consists of 64 elements, which each of them is quartz Cherenkov counter. BBC have four major tasks, to trigger the Minimum Bias events, to measure the collision vertex, to obtain the collision time and determine centrality. In addition, the reaction plain is determined by hit pattern of BBC. The collision vertex and time are determined by the difference and average time to north and South counters;

$$collision\ vertex = \frac{(T_S - T_N)}{2} \times c \tag{2.1}$$

$$collision\ time = \frac{T_S + T_N - (2 \times L)/c}{2} \tag{2.2}$$

where T_N and T_S are the averaged hit time of incoming particles, c is the light velosity and L is the distance from $z = 0$ to both BBCs, $L = 144.35$ cm.

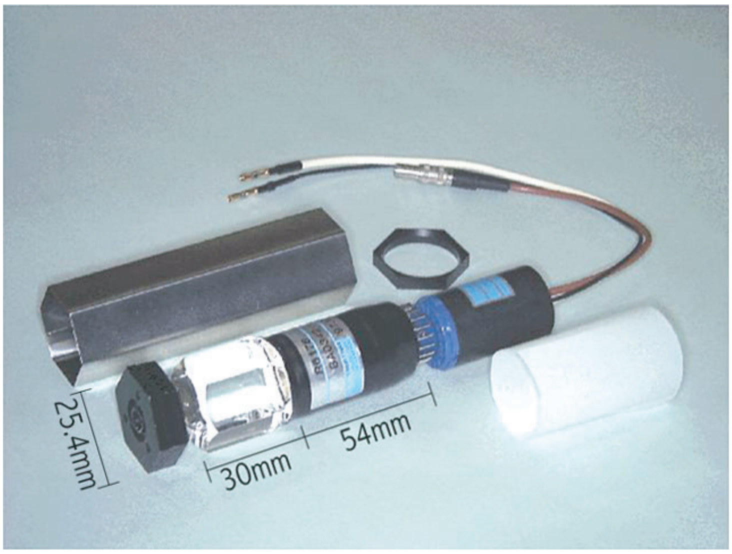

Figure 2.3: picture of the one element of Beam-Beam Counter

2.3.2 Zero Degree Counters (ZDC)

Zero Degree Calorimeters(ZDC) [18] are hadron calorimeter located at 18m North and South side along beam pipe from the collision point. Since the both north and south ZDC sit at just the upstream of the last bending magnet on the RHIC ring, most of charged particles are swept out from the acceptance. So, ZDC works as the minimum bias trigger counter and monitor the beam luminosity since ZDC measured neutrons from spectator part of heavy ion collision.

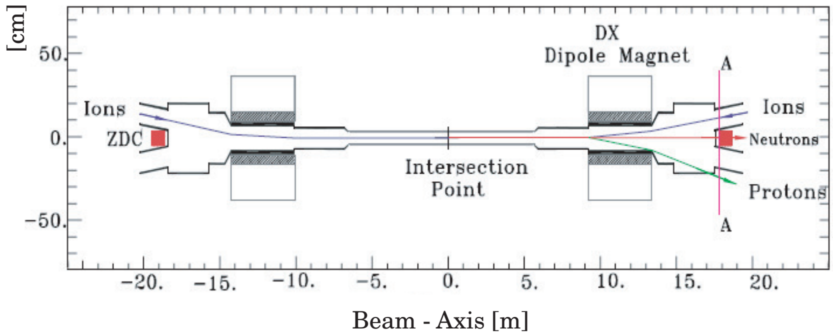

Figure 2.4: schematic view of the ZDC location including deflection of protons and charged fragments

2.4 Magnet

The PHENIX has three magnet systems [19], one is the central magnet, others are north and south muon magnets. The central magnet provide a magnetic field around the collision point which is parallel to the beam. And the Central magnet consist of inner and outer coil, which can be optimized separately, together, or in opposition. During the run for this work, both inner and outer magnets are energized and integrated magnetic field is 1.15 $T \cdot m$. the momentum of charged particles can be obtained by measuring the curvature of the track which is bended due to magnetic field.

2.5 Central Arm Detectors

The central arm detectors can measure charged hadron, electron and photon, and consists of three parts : the tracking system , particle identification system and electro magnetic calorimeter. The Drift Chamber(DC) and Pad Chamber(PC) form the tracking unit and measures the momentum of charged particles from collisions. The Ring-Imaging Cherenkov(RICH) and the Time-of-Fight(ToF) provide identification of charged particles. Additionally, Electro Magnetic Calorimeter(EMCal) is used to measure the spatial position and energy of electrons and photons.

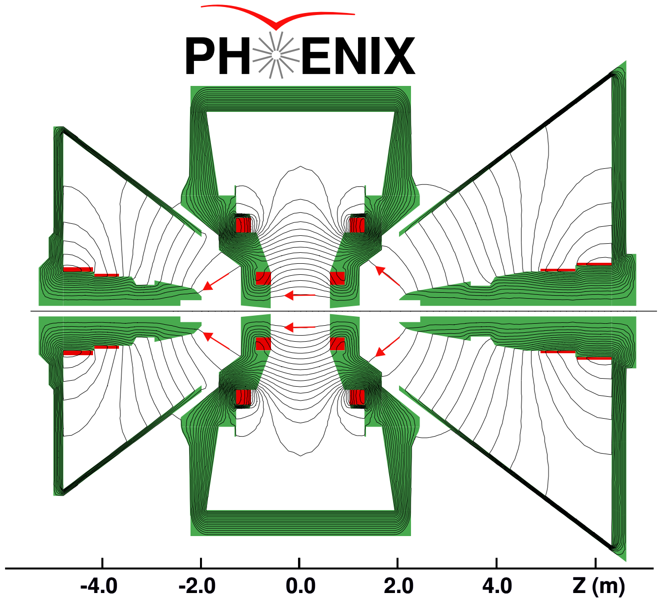

Figure 2.5: overview of the Magnet [27]

2.5.1 Drift Chamber (DC)

The Drift Chambers(DC) are cylindrically shaped and located in the region from 2 to 2.4 m from the beam axis and 2 m along the beam axis. This places them in a residual magnet field with a maximum of 0.6 kG. Fig.2.11 is shown position of DCs relative to the other detectors. Each DC measures charged particle trajectories to determine transverse momentum of each particles. The DC also participates in the pattern recognition at high particle track densities by providing position information that is used to link tracks thought the various PHENIX detectors.

2.5.2 Pad Chamber (PC)

The PHENIX Pad Chambers(PC) are multiwire proportional chambers that form three separate layers. Each detectors consists of a single plane of wire inside a gas volume bounded by two cathode plane. One cathode is finely segmented int an array of pixels. The charge induced on a number of pixels when a charged particle starts an avalanche on an anode wire, is read out thorough specially designed read out electronics. The PC system determines space points along the straight line particle trajectories outside the magnetic field. Fig.2.11 shows position of PCs relative to the other detectors. The innermost pad chamber called PC1 is essential for determining the three-dimensional momentum vector by providing the z coordinate at the exit of the DC.

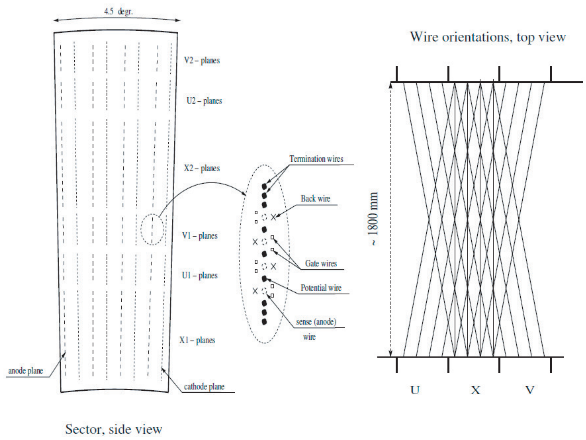

Figure 2.6: The layout of wire position of DC. The X1 and X2 wire cells runs in parallel to the beam to perform precise track measurements in r-ϕ. U1, V1, U2, V2 wires have stereo angle of about 6° relative to the X wires and measure the z coordination of track.

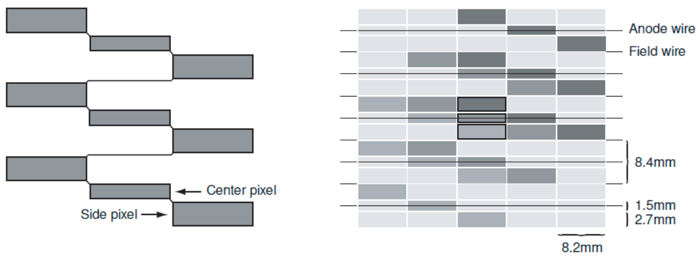

Figure 2.7: the pad and pixel geometry(left), A cell defined by three pixels is at the center of the right picture.

2.5.3 Ring Image Cherenkov Counters (RICH)

The Ring Image Cherenkov Counters(RICH) [22] is occupies the radial region between 2.575 and 4.1 m from the beam line. Each of the detectors in the east and west central arms has a volume of 40cm^2. the minimum thickness of the radiator gas, which is CO_2, is 87 cm, the maximum is about 150 cm. The RICH is provides e/π discrimination below the π Cherenkov threshold, which is set at 4.65 GeV/c. The Cherenkov photon produced in the radiator gas are reflected on the mirror and are detected by the photon multiplier tubes (PMTs). The average size of the Cherenkov ring is 8 cm and average number of the Cherenkov photon produced by electron is 10.8 on the plane where the PMTs are sitting. Fig.rich show the cut through view of RICH detector.

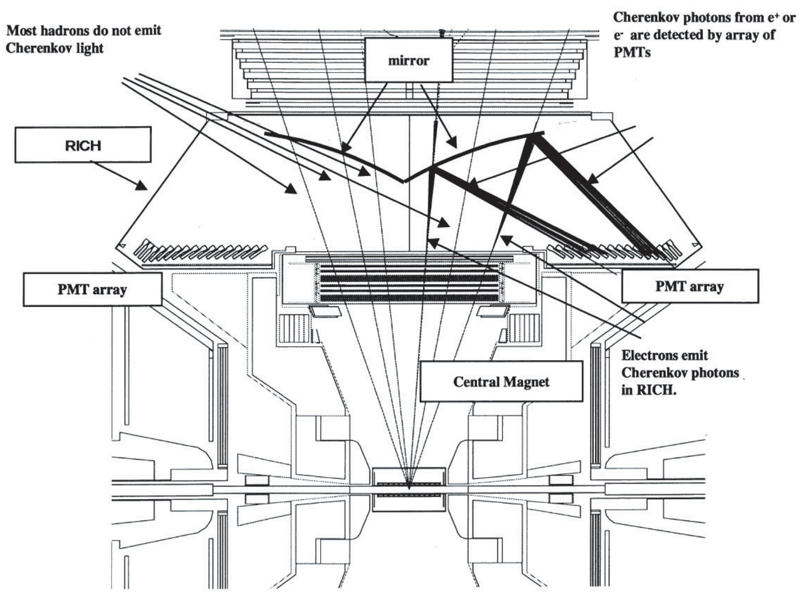

Figure 2.8: A cut through view of RICH detector

2.5.4 Electro Magnetic Calorimeter (EMC)

The Electro Magnetic Calorimeter (EMCal) is designed primarily to measure the energies and spatial position of photon and electrons. It also plays a major role of in particle identification and is an important part of the PHENIX trigger system. The EMCal system can trigger on rare events with high transverse momentum photons and electrons. The EMCal system consists of a total of 24768 individual detector modules divided between the Pb-Scintillator calorimeter (PbSc), which provides 6 sectors of central arm and the Pb-Glass calorimeter (PbGl) comprised of 2 sectors.

The PbSc is a sampling calorimeter made of alternating tile of Pb and scintillator consisting of 15552 individual towers and covering an area of approximately 48 m^2. The basic block is a module consisting of 4 towers, which are optically isolated, and are read out individually. The tower has 5.52×5.25 cm^2 cross section and 3.75 cm in length. Figure 2.9 show the interior view of the module. A super-module is composed of 12×12 towers and a sector is composed of $18(12\times12)$ super-modules.

The PbGl is a Cherenkov type calorimeter. A lead glass has 4.0×4.0 cm^2 cross section and 40 cm length. Figure 2.10 shows the interior view of one super-module, composed by 4×6 towers. A sector is composed of $192(12\times12)$ super-modules.

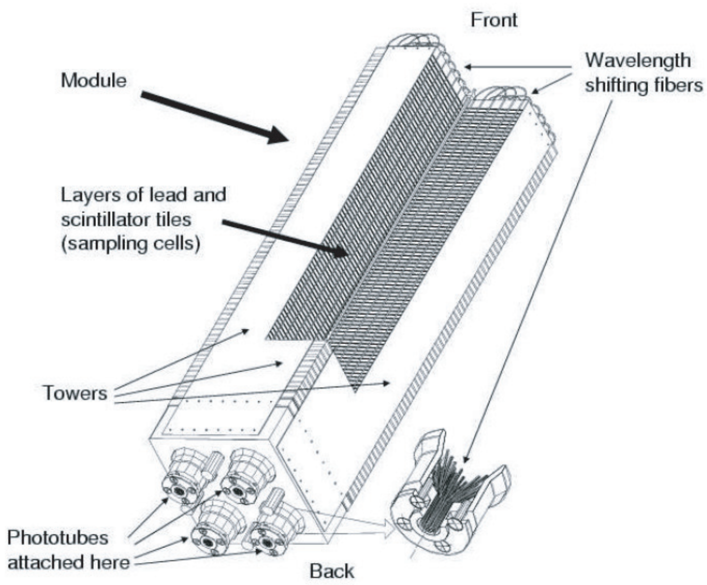

Figure 2.9: Interior view of a lead-scintillator calorimeter module

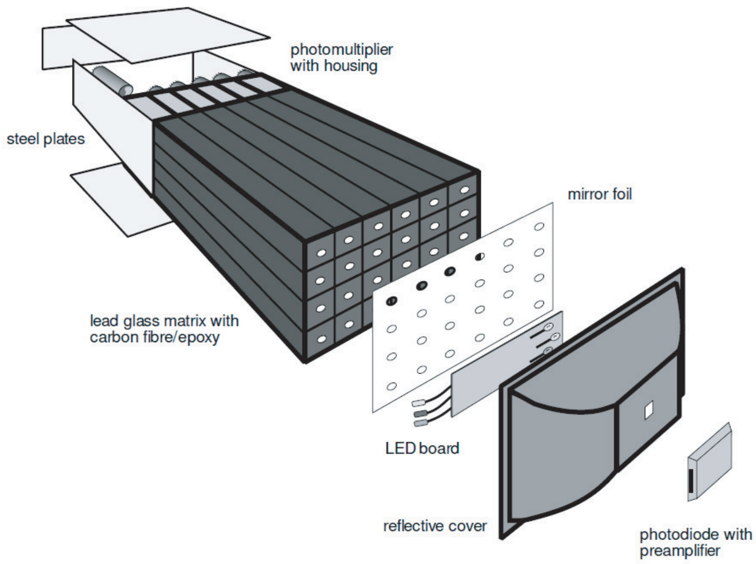

Figure 2.10: Exploded view of a lead-glass detector supermodule

2.6 Computing

2.6.1 Overview of Data Acquisition system (DAQ)

PHENIX is designed to make measurements on a variety of collision system from p+p to Au+Au. The occupancy in the detector varies from a few tracks in p+p interaction to approximately 10% of all detector channels in central Au+Au interactions. The interaction rate at design luminosity varies from a few kHz for Au+Au central collisions to approximately 500 kHz for minimum bias p+p collisions. The PHENIX DAQ system was designed to seamlessly accommodate improvements in the design luminosity. This was accomplished through the pipelined and deadtimeless features to the detector front ends and the ability to accommodate higher-level triggers.

In PHENIX it is necessary to measure low-mass lepton pair and low p_T particles in a high-background environment. In order to preserve the high interaction-rate capability of PHENIX a flexible system that permits tagging of events was constructed. The On-Line system has two levels of triggering denoted of LVL1 and LVL2. The LVL1 trigger is fully pipelined, therefore the On-Line system is free of deadtime through LVL1. Buffering is provided that is sufficient to handle fluctuations in the event rate so that deadtime is reduced to less than 5% for full RHIC luminosity. The LVL1 trigger and lower levels of the readout are clock-driven by bunch-crossing signals from

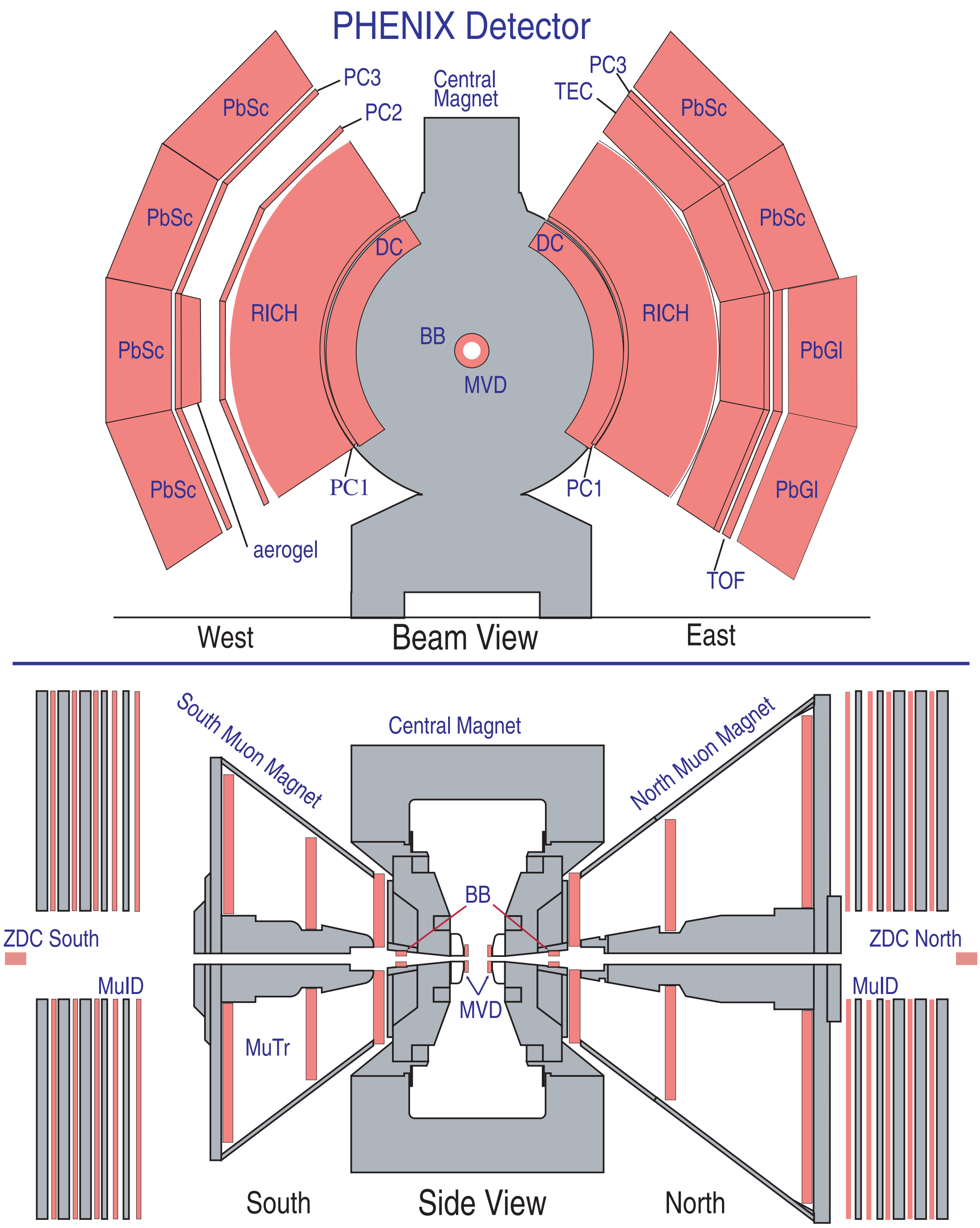

Figure 2.11: The PHENIX Detector configuration [27]

the 9.4 MHz RHIC clock. The higher levels of readout and the LVL2 trigger are data-driven where the results of triggering and data processing propagate to the next higher level only after processing of a given event is completed.

The general schematic for the PHENIX On-Line system is shown in Fig. 2.12. Signals from the various PHENIX subsystems are processed by Front End Electronics (FEE) that convert detector signals into digital event fragments. This involves analog signal processing with amplification and shaping to extract the optimum time and/or amplitude information, development of trigger input data and buffering to allow time for data processing by the LVL1 trigger and digitization. This is carried out for all detector elements at every beam crossing synchronously with the RHIC beam clock. The timing signal is a harmonic of the RHIC beam clock and is distributed to the FEM's by the PHENIX Master Timing System (MTS). The LVL1 trigger provides a fast filter for discarding empty beam crossings and uninteresting events before the data is fully digitized. It operates in a synchronous pipelined mode, generates a decision every 106 ns and has an adjustable latency of some 40 beam crossings.

Once an event is accepted the data fragments from the FEM's and primitives from the LVL1 trigger move in parallel to the Data Collection Modules (DCM). The PHENIX architecture was designed so that all detector-specific electronics end with the FEM's, so that there is a single set of DCM's that communicate with the rest of the DAQ system. The only connection between the Interaction Region (IR) where the FEM's are located and the Counting House (CH) where the DCM's are located is by fiber-optic cable. The DCM's perform zero suppression, error checking and data reformating. Many parallel data streams from the DCM's are sent to the Event Builder (EvB). The EvB performs the final stage of event assembly and provides an environment for the LVL2 trigger to operate. In order to study the rare events for which PHENIX was designed, it is necessary to further reduce the number of accepted events by at least a factor of six. This selection is carried out by the LVL2 triggers while the events are being assembled in the Assembly and Trigger Processors (ATP) in the EvB. The EvB then sends the accepted events to the PHENIX On-line Control System (ONCS) for logging and monitoring. The logged data, which is named as PHENIX Raw Data File(PRDF), are send to RHIC Computing Facility(RCF) for sinking on the tape in High Performance Storage System(HPSS). The data in the HPSS are analyzed and converted into an intermediated data format in the linux computer at RCF and Computing Center in Japan(CCJ).

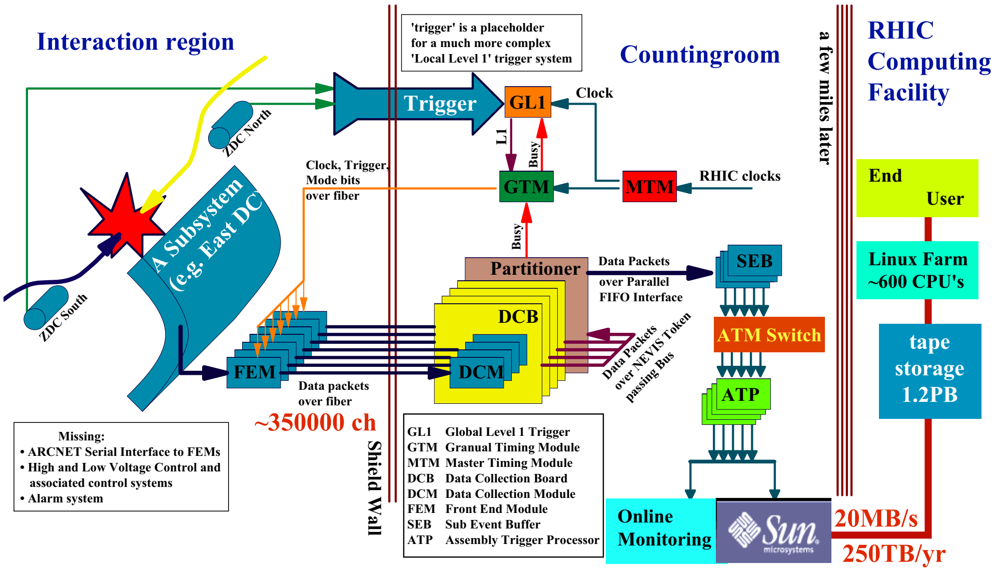

Figure 2.12: block diagram of DAQ [27]

2.6.2 EMCal RICH level 1 Trigger

the PHENIX has had two kinds of the Level 1 trigger. One is minimum bias trigger which is require at least one hit on the north and south BBCs. The other is the EMCcal RHIC level 1 trigger(ERT) designed to enhance the electron, positron, pair of electron and positron pair, high p_T charged particles, and π_0. The ERT is crucial for measurement of e^+e^- pair due to the rare events including e^+e^- pairs. For enhancement of the e^+e^- pair sampled events, the information of RICH and EMCal is used. For this analysis, the ERT requires RICH coincidence with EMCal. The ERT trigger threshold of 400MeV is required for EMCal to discriminate high p_T charged pion since the charged pion only deposit the minimum ionized energy into EMCal. The schematic view of ERT is shown Figure 2.13.

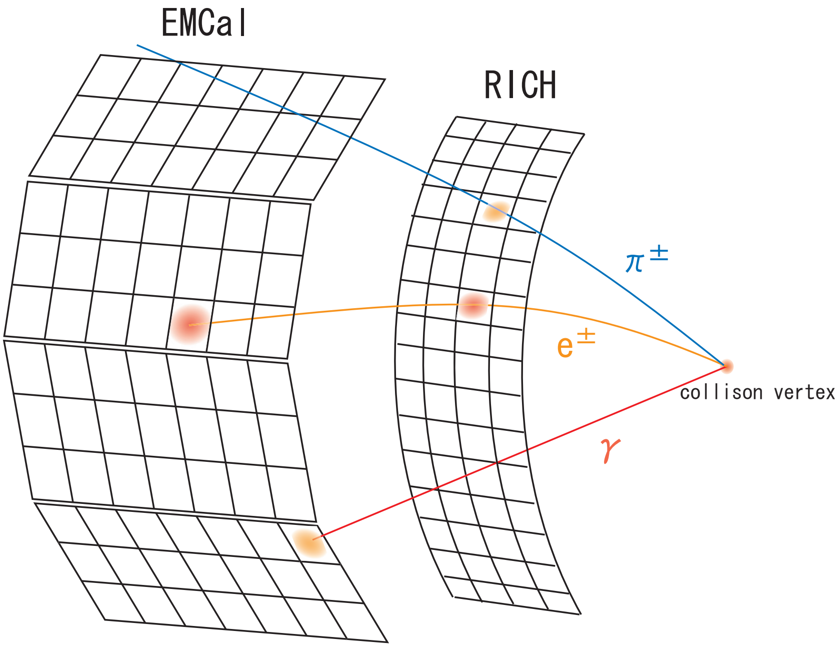

Figure 2.13: schematic view of EMCal RICH level1 Trigger: Both the super-Module of EMCal and RICH are fired for e^+,e^-. Only the EMCal is fired for photon, while only the RICH is fired for high p_T pion. We are able to effectively collect the events including e^+e^- pair.

Chapter 3

Analysis

3.1 Data Set

the PHENIX collected the date at proton + proton collisions in year 2005. The Run number in proton + proton collisions is from 166030 to 179846. In this analysis, we used 16,587 nDST(Data Summary Tape) files were made from PRDF. The total data size of the nDST is approximately 410 *GBite*.

3.2 Event Selection

The electron yield, which is defined in Eq.3.1 , for each run number is checked.

$$N_e \times N_p = N_e/N_{evt} \times N_p/N_{evt} \tag{3.1}$$

where N_e,N_p and N_{evt} in right term are the number of electrons, the number of positrons and the number of MinBias events, respectively. Figure.3.2 shows $N_e \times N_p$ as function of run number. The electron yield drops after run 178937 since two of RICH data packets were disable after this run.

The analysis is restricted to events with collision vertex fulfilling $|bbcz|$ < 25 cm, where *bbcz* is the vertex position found by the BBC. The collision vertex distribution is shown Figure 3.1. After these run selection and global cut, 56.39 M minimum bias sampled events are used in this analysis.

3.3 Track selection and electron identification

3.3.1 Track Quality

The following track quality selection is applied:

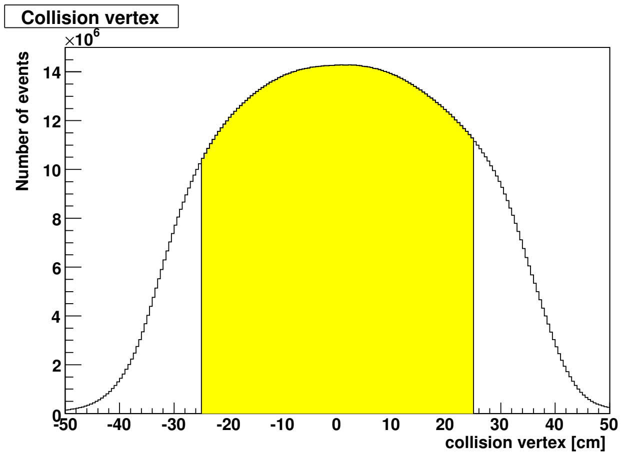

Figure 3.1: Collision vertex distribution measured by beam detector. The events in yellow band range are selected for this analysis.

- quality bits = 31 ∪ 63

the value of 31 means the tracks are required the hit of X1,X2 wire and unique hit of UV wire, in addition, hit of PC1. the case of 63, tracks are additionally required the unique hit of PC1.

3.3.2 Fiducial cut

To reduce the systematic uncertainly for the acceptance, dead and unstable areas of DC and EMCal are removed [35]. Figure 3.3 shows the areas removed due to dead and unstable of DC. Figure 3.4 shows the areas removed due to dead and warm for sector-by-sector of EMCal. In addition that, dead areas of PC1 are removed.

3.3.3 eID parameters

Electrons are identified with RICH and EMCal. The variables which are used for electron identification are summarized in Table 3.1. In this analysis, the following cuts are applied:

- number of fired PMT's shown as Fig.3.5: $n0 > 2$
- track matching to RICH shown as Fig.3.6: $disp < 5$ cm
- energy-momentum matching shown as Fig.3.7: $|dep| < 3\sigma$

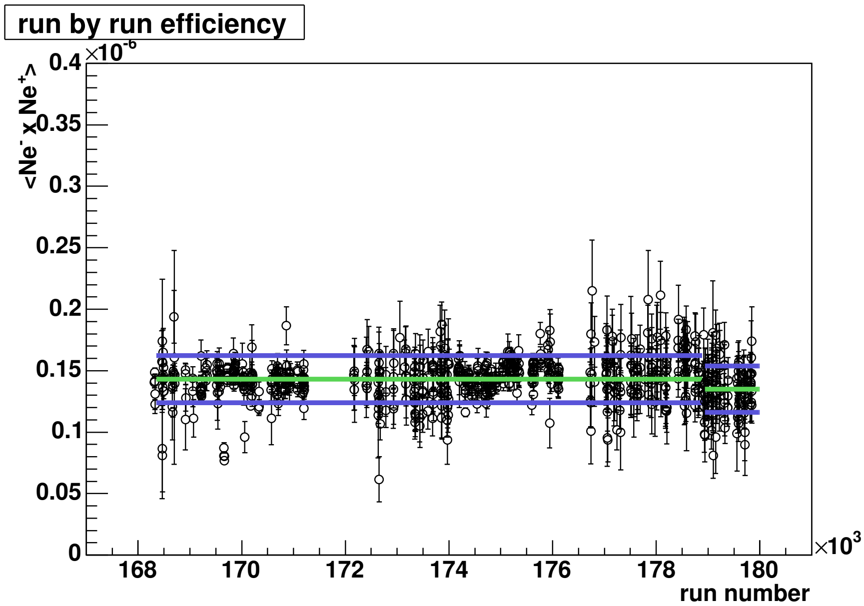

Figure 3.2: $N_e \times N_p$ as function as run number. The Green line is the mean of $N_e \times N_p$, and blue line is its RMS.

- track matching to EMCal shown as Fig.3.8, 3.9: $\sqrt{emcsdphi^2 + emcsdz^2} < 4\ \sigma$

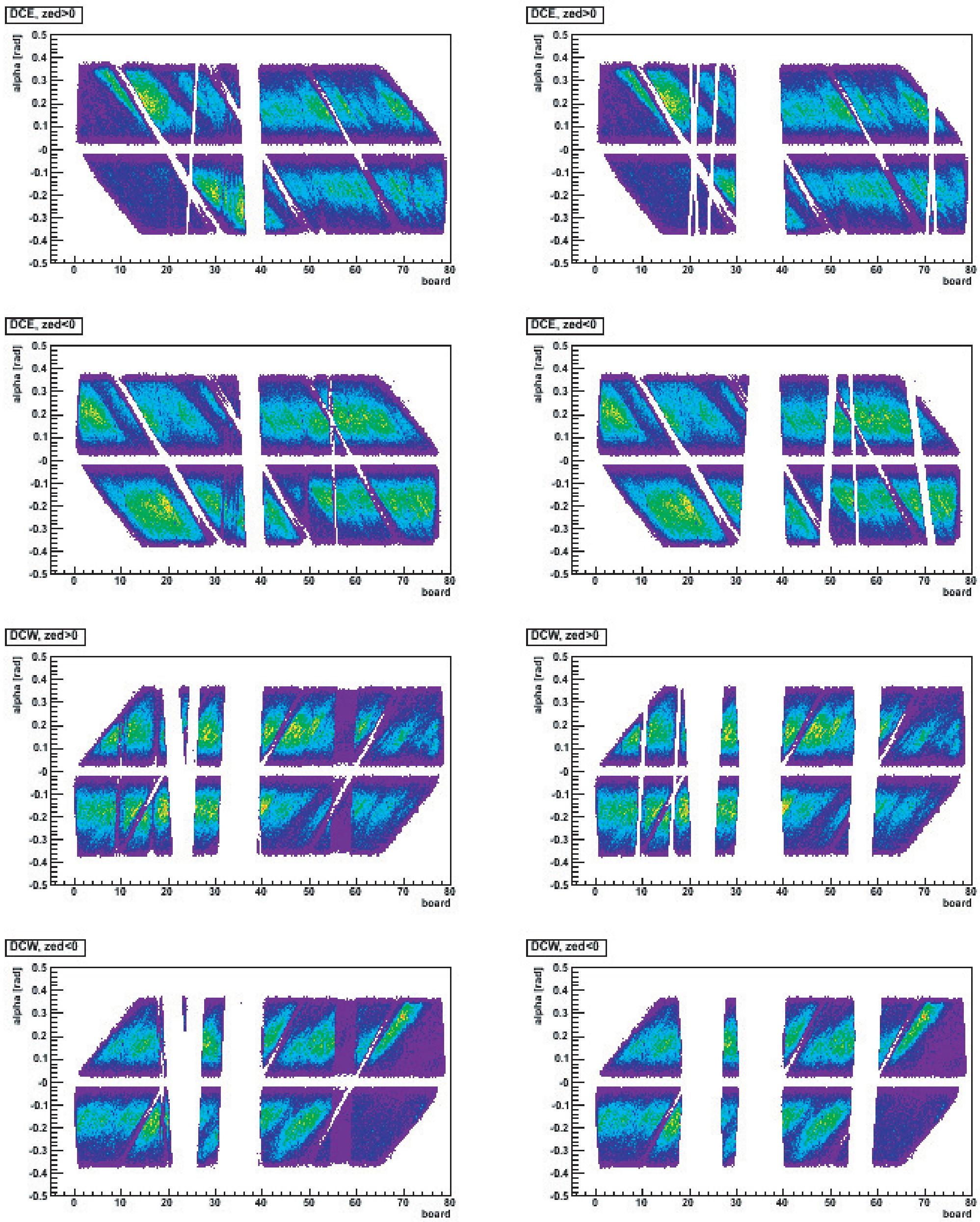

Figure 3.3: Alpha versus bord distribution for both side of the DC east and DC west. The left and right figures show before and after removing the dead and unstable regions, respectively.

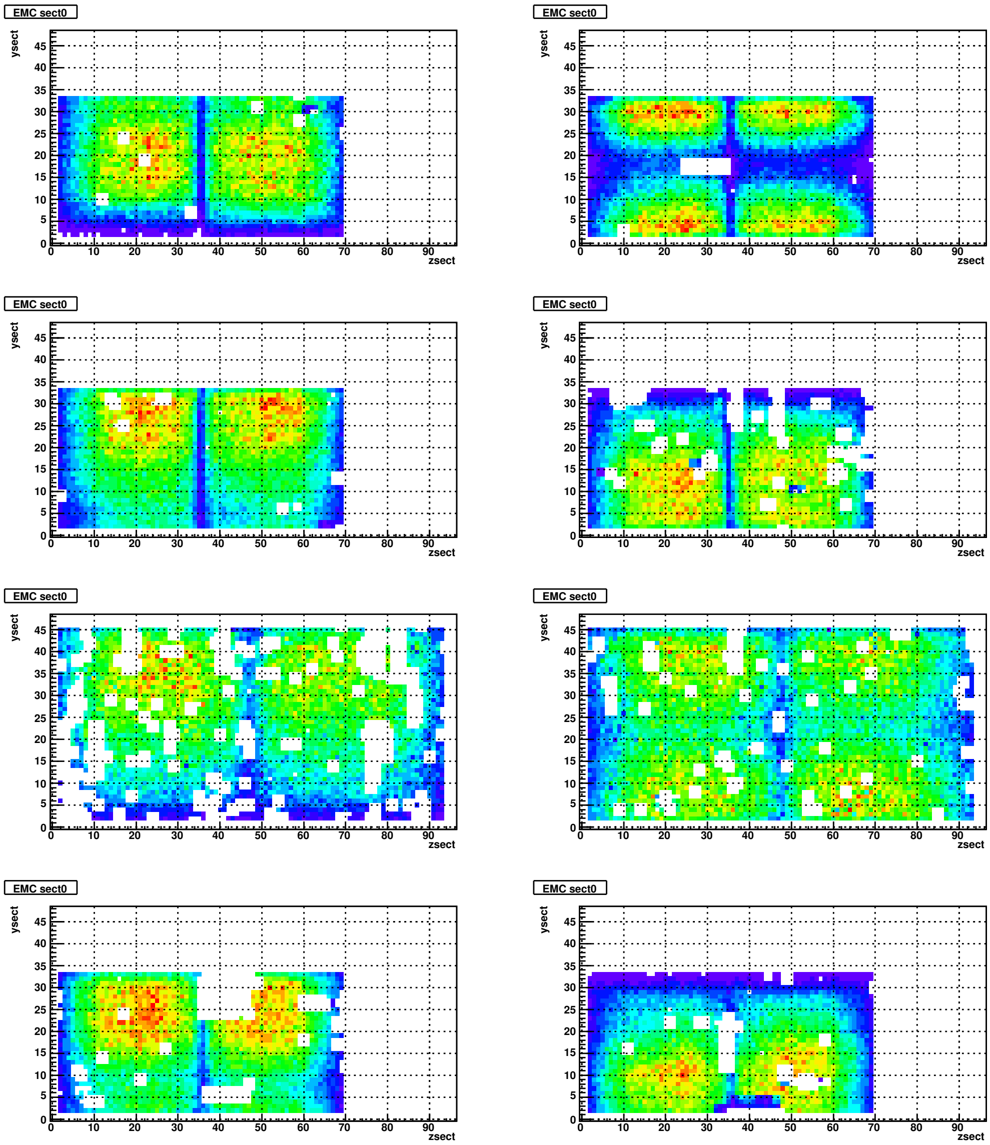

Figure 3.4: Hot and dead map. The blank area is removed in this analysis

variable	description
$n0$	number of fired PMT's in nominal ring radius
$disp$	displacement between the projection point onto RICH PMT plane and the ring center reconstructed from the fired PMT's
$ecore$	energy detected at EMCal (summed up for 3 towers)
mom	transverse momentum by DC
$emcsdphi$	track matching in phi direction at EMCal surface normalized by σ
$emcsdz$	track matching in z direction at EMCal surface normalized by σ
dep	$ecore/mom$ -1 normalized by $\sigma(mom)$

Table 3.1: eID parameters list

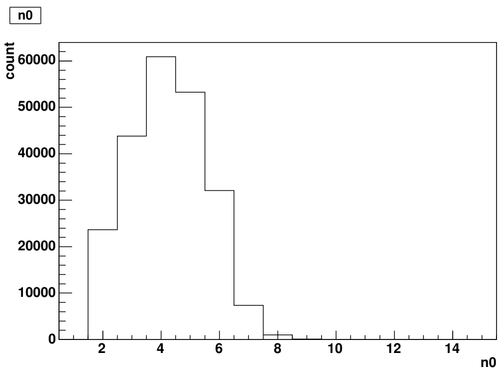

Figure 3.5: distribution of number of fired PMT's on RICH

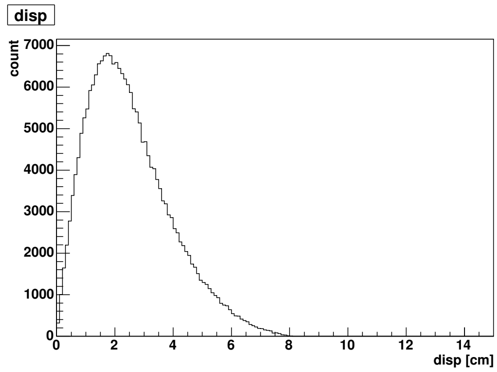

Figure 3.6: distribution of the displacement between projection and reconstructed ring center

3.3.4 DC ghost track rejection

Ghost tracks in the DC are rejected as follows. If any two tracks fulfill $|DC^1_{zed} - DC^2_{zed}| < 0.5$ cm and $|DC^1_{phi} - DC^2_{phi}| < 0.02$ rad, the one with worse EMCal matching is rejected, as it is likely to be a ghost track.

3.3.5 RICH ring sharing rejection

Two tracks share the same RICH ring when they are parallel to each other while passing through the RICH gas. In this case, one of them is possibly a misidentified hadron. The RICH ghosting phenomenon decreased purity of electron and also made correlation in the invariant mass spectrum around 0.5 GeV/c^2. So that such tracks need to be rejected. Fig.3.11 shows correlation

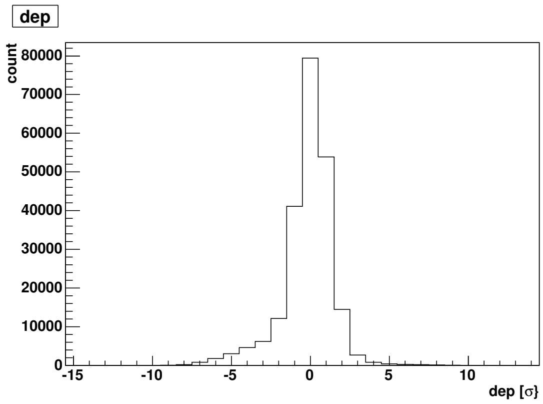

Figure 3.7: distribution of E/p -1 normalized by its σ. E means energy deposited into EMCal, and p means particle momentum.

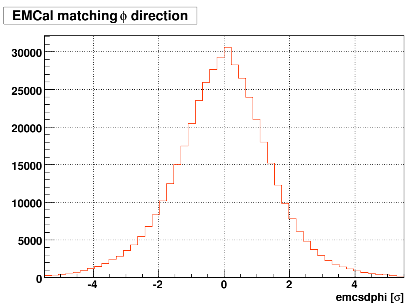

Figure 3.8: distribution of track matching in ϕ direction normalized by its σ

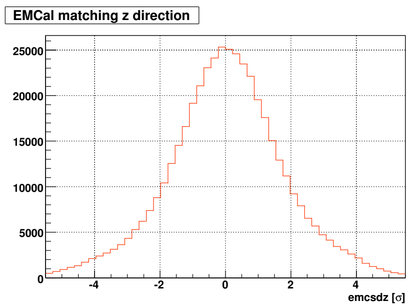

Figure 3.9: distribution of track matching in z direction normalized by its σ

between PFOA and $dCROSS$. If any two tracks fulfill $|dCROSS| < 3\ \sigma$ and PFOA < 0.25 rad, both of the tracks are rejected. PFOA(Post-Field Opening Angle) is the angle between two track vector after they have been deflected by the PHENIX magnet. $dCROSS$ is defined following.

$$dCROSS \equiv \sqrt{(|RICH_z^1 - RICH_z^2|/9.55)^2 + (|RICH_{phi}^1 - RICH_{phi}^2|/0.023)^2}$$

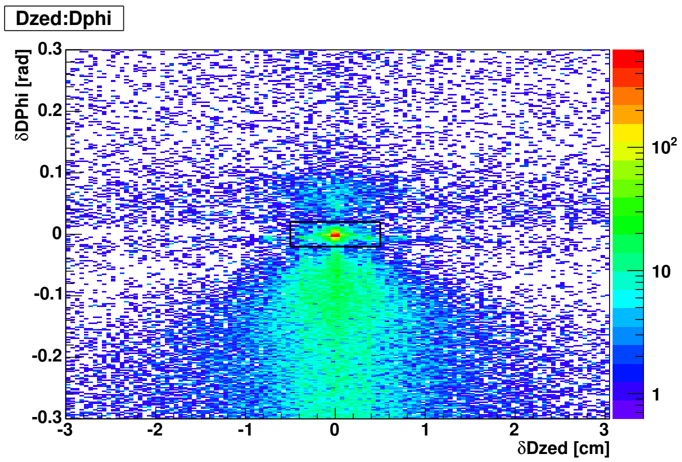

Figure 3.10: GhostTracks

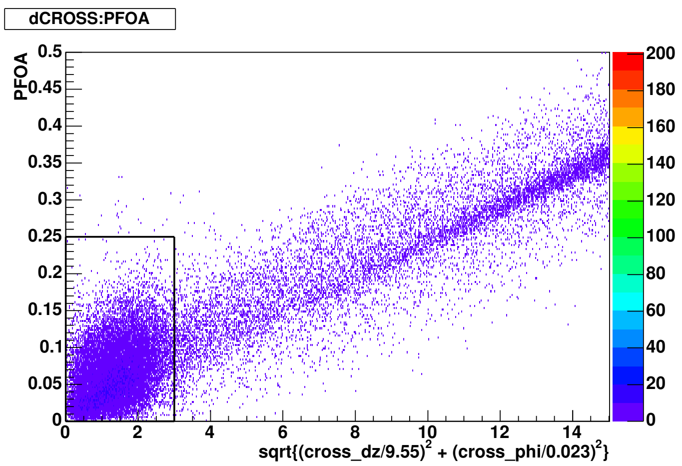

Figure 3.11: ring sharing tracks.

3.4 Signal Extraction

3.4.1 Pair reconstruction

The invariant mass M_{ee} is written as,

$$M_{ee} = \sqrt{(E_{e^+} + E_{e^-})^2 - (\vec{p_{e^+}} + \vec{p_{e^-}})^2} \tag{3.2}$$

where E is the energy of the particle, $\vec{p}$ is particle momentum,

$$(E_{e^+} + E_{e^-})^2 = (\sqrt{m_{e^+}^2 + p_{e^+}^2} + \sqrt{m_{e^-}^2 + p_{e^-}^2})^2 \tag{3.3}$$

and,

$$(\vec{p_{e^+}} + \vec{p_{e^-}})^2 = (p_{e^+x} + p_{e^-x})^2 + (p_{e^+y} + p_{e^-y})^2 + (p_{e^+z} + p_{e^-z})^2. \tag{3.4}$$

p_x, p_y, p_z is written as following,

$$\begin{aligned} p_x &= p \times \sin\theta \cos\phi \\ p_y &= p \times \sin\theta \sin\phi \\ p_z &= p \times \cos\theta \end{aligned}$$

where θ is the poler angle measured from the beam axis and ϕ is the azimuthal angle.

The invariant mass spectrum were derived by combination all identified e^+e^- pairs. The reconstructed invariant mass spectrum is divided 6 p_T bins, such as $0<p_T<0.5$, $0.5<p_T<1.0$, $1.0<p_T<1.5$, $1.5<p_T<2.0$, $2.0<p_T<3.0$, $3.0<p_T<4.0$.

3.4.2 background subtraction

Invariant mass of any e^+e- pairs in each event was calculated. Then, to evaluate the mass shape and the number of ω and ϕ, it is necessary to subtract the background from invariant mass spectrum. The source of the background is listed as following.

- Uncorrelated e^+e^- pairs. (combinatorial background)
- Corrected e^+e^- pair from $D\bar{D}$, $B\bar{B}$ and Drell-Yan production. (continuum yield)

In this analysis, the background from continuum yield are ignored since the main source of the background on the mass region of ω and ϕ is from combinatorial background. Event mixing technique is used to subtract the combinatorial background. Figure 3.12 shows a schematic view of the event mixing technique. The uncorrelated e^-e^+ pairs are produced by using the e^- (e^+) in current event and the e^+ (e^-) in other events. Figure 3.13 show the invariant mass spectrum with combinatorial background evaluated by event mixing technique. The mass spectra divided into p_T bins are shown in Fig.3.14 .

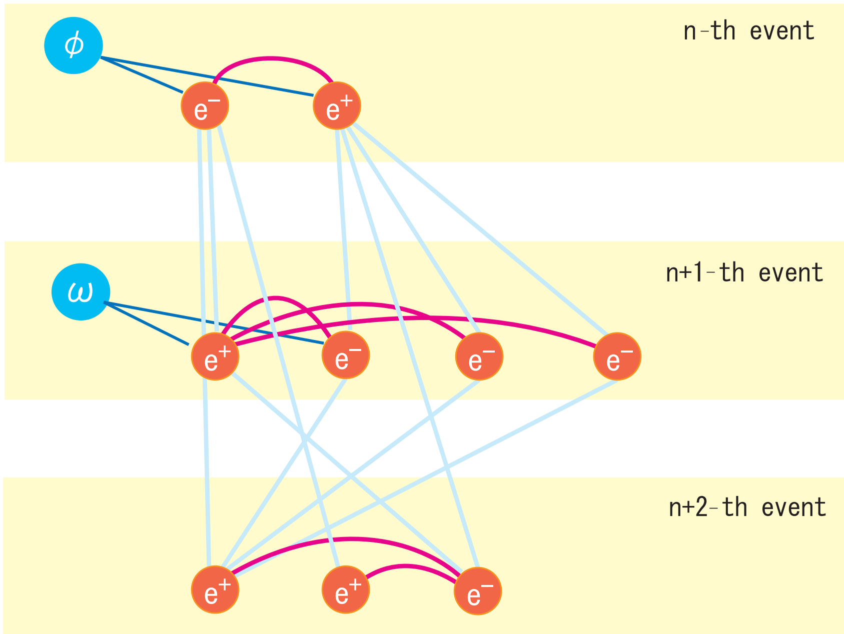

Figure 3.12: schematic of reconstruction: the solid magenta and light blue lines show the reconstruction process in "same event" and "event mixing", respectively.

3.4.3 Spectral Shape of Resonances

Spectral shape of resonances were generated using the relativistic Breit-Winger distribution [28]

$$rBR(m) = \frac{m^2\Gamma_{tot}(m)\Gamma_{ee}(m)}{(m^2 - m_0^2)^2 + m_0{}^2\Gamma_{tot}(m)^2} \tag{3.5}$$

with the pole mass, m_0, total decay width, $\Gamma_{tot}(m)$ and the energy dependent partial decay width of the vector meson going to e^+e^-, $\Gamma_{ee}(m)$.

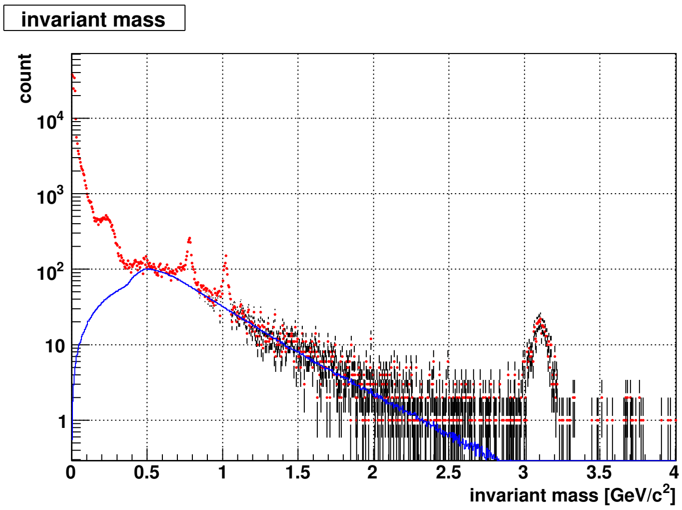

Figure 3.13: invariant e^+e^- mass spectrum. The blue line indicate combinatorial background evaluated by the event mixing method.

$\Gamma_{tot}(m)$ and $\Gamma_{ee}(m)$ can be parametrized as

$$\Gamma_{tot}(m) = \frac{m}{m_0}\Gamma_{tot} \quad (3.6)$$

$$\Gamma_{ee}(m) = \frac{m_0^3}{m^3}\Gamma_{ee} \quad (3.7)$$

$$(3.8)$$

where Γ_{tot} is the natural decay width, Γ_{ee} is the partial width of the vector meson decaying into e^+e^-. The values of the natural decay widths and pole masses of vector masons are shown in table 3.2

	mass $[MeV/c^2]$	Γ_{tot} $[MeV/c^2]$	Γ_{ee}/Γ_{tot}
ρ	771.1	149.2	0.454×10^{-4}
ω	782.57	8.44	0.695×10^{-4}
ϕ	1019.456	4.26	2.96×10^{-4}

Table 3.2: The pole masses and natural decay widths of the vector mesons taken from the PDG [29]

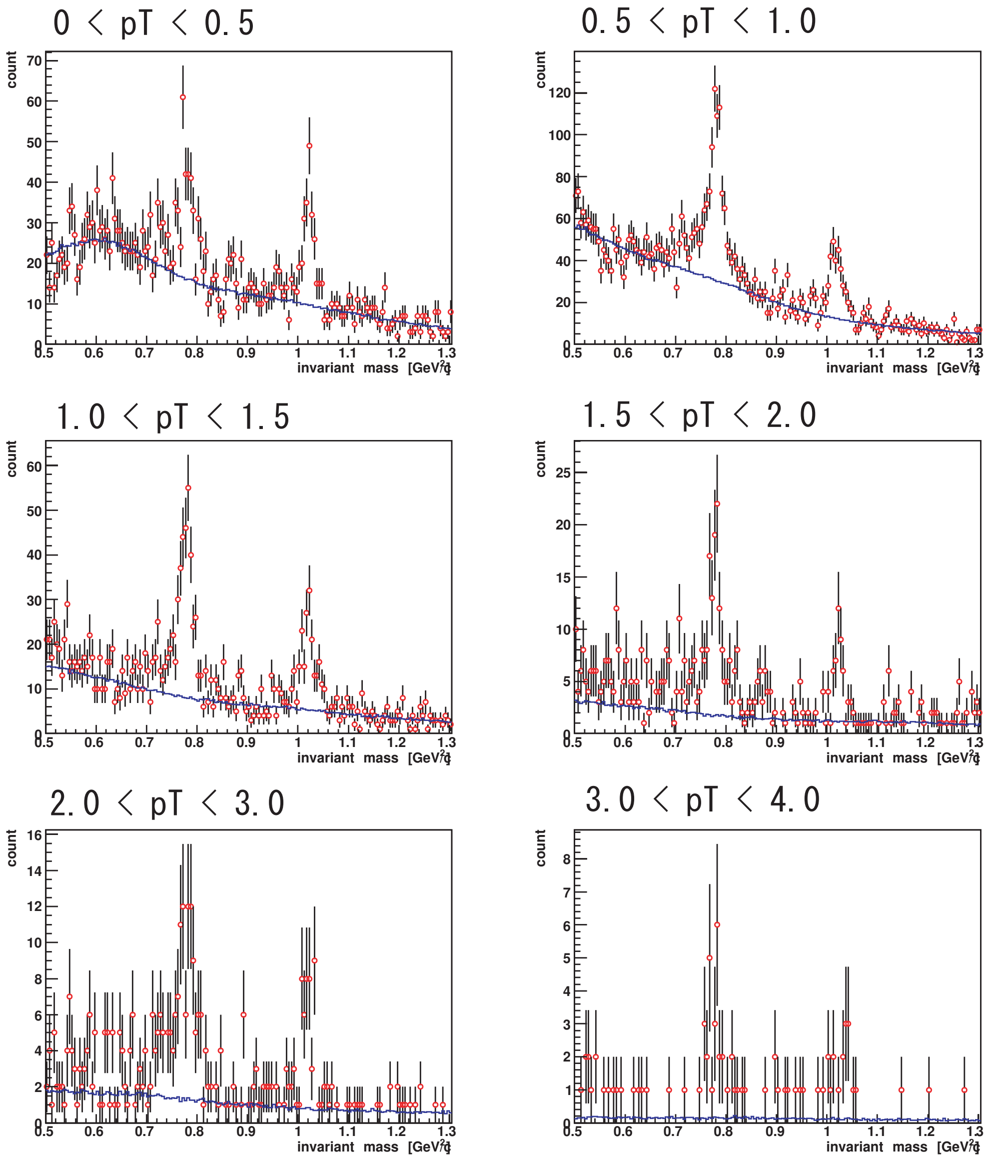

Figure 3.14: Invariant mass spectra divided by pT bins. The blue line indicate combinatorial background evaluated by the event mixing method.

3.4.4 Radiative tail correction

The radiative correction to e^+e^- was estimated. The observation of radiative decays $J/\psi \to e^+e^-\gamma$ was reported and the result is consistent with a QED calculation based on final state radiation [30]. The radiative decay is described by the diagrams shown Figure 3.15.

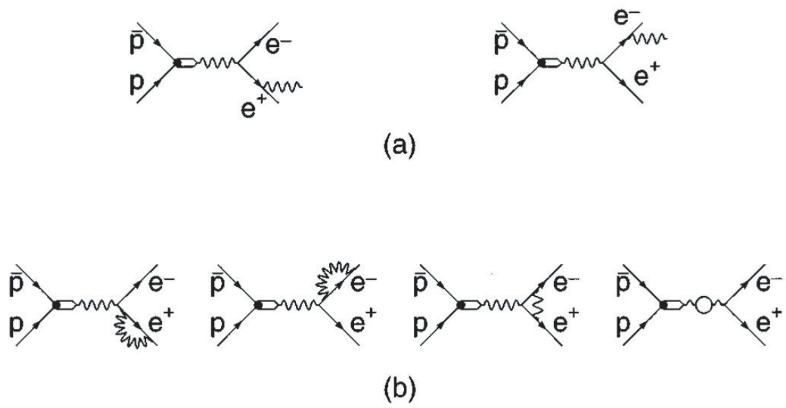

Figure 3.15: Diagrams for final state radiation [30]. The decay into $e^+e^-\gamma$ is described by (a). The infrared divergence in the decay is canceled by interference with the diagrams in (b).

An analytic formula for the di-lepton mass spectra in radiative decays is derived [31]. The fraction of decays corresponding to the emission of hard photons is

$$C_{hard} = \frac{\alpha}{2\pi}\left[4\ln\frac{M}{2E_{min}}\left(\ln\frac{M^2}{m_l^2} - 1\right) - 3\ln\frac{M^2}{m_l^2} - \frac{2}{3}\pi^2 + \frac{11}{2}\right] \tag{3.9}$$

where E_{min} is the minimal photon energy, M is a mass of parent particle and m_l is a mass of leptons. The di-lepton mass m is shifted by photon emission

$$m = \sqrt{M(M - 2E_\gamma)} \approx M - E_\gamma(E_\gamma \leq M) \tag{3.10}$$

Hard photon emission cause a tail towards lower mass in the di-lepton mass spectrum. The distribution $P(m)$ of the di-lepton mass in the radiative decay is described as

$$P(m) = \frac{\alpha}{\pi}\frac{2m}{(M^2 - m^2)}\left(1 + \frac{m^4}{M^4}\right)\left(\ln\frac{1+r}{1-r} - r\right) \tag{3.11}$$

where $r = \sqrt{1 - 4m_l^2/m^2}$ is also a function of m. Figure 3.16 shows the mass spectra in the radiative decay $\phi \to e^+e^-\gamma$ for $E_{min} = 10\text{MeV}$.

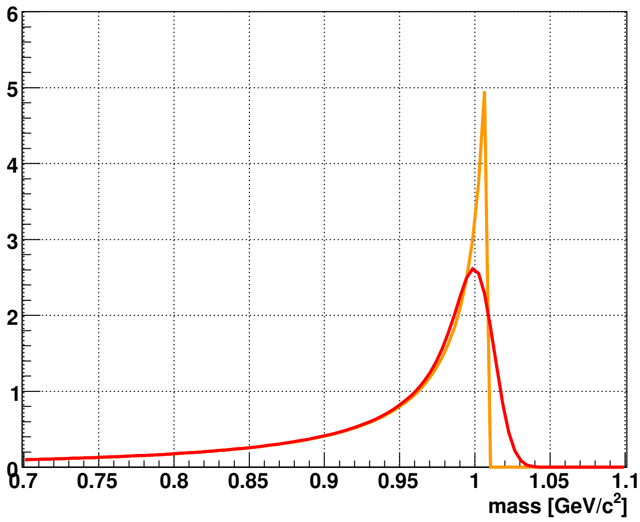

Figure 3.16: e^+e^- mass spectrum in the radiative decay $\phi \to e^+e^-\gamma$ for E_{min} = 10MeV(orange) smeared with 10MeV(red).

3.4.5 Signal Counting

Fitting function consists of

Gaussian convoluted r.BW + radiative tail + Breit-Wigner.

The first term and second term is for ω and ϕ mesons. The third term, Breit-Winger, is for ρ mesons. The number of ω and ϕ mesons are obtained by the first and second term. The fitting parameters are the peak amplitude, mass center and experimental mass resolution, while the width Γ_{tot} are fixed to PDG value [29]. The ratio between the number of ρ and ω are fixed. The ρ /ω ratio is fixed to 1.53, which obtained by ration of branching into e^+e^-

The fitting result for invariant mass spectra are shown in Fig.3.17.

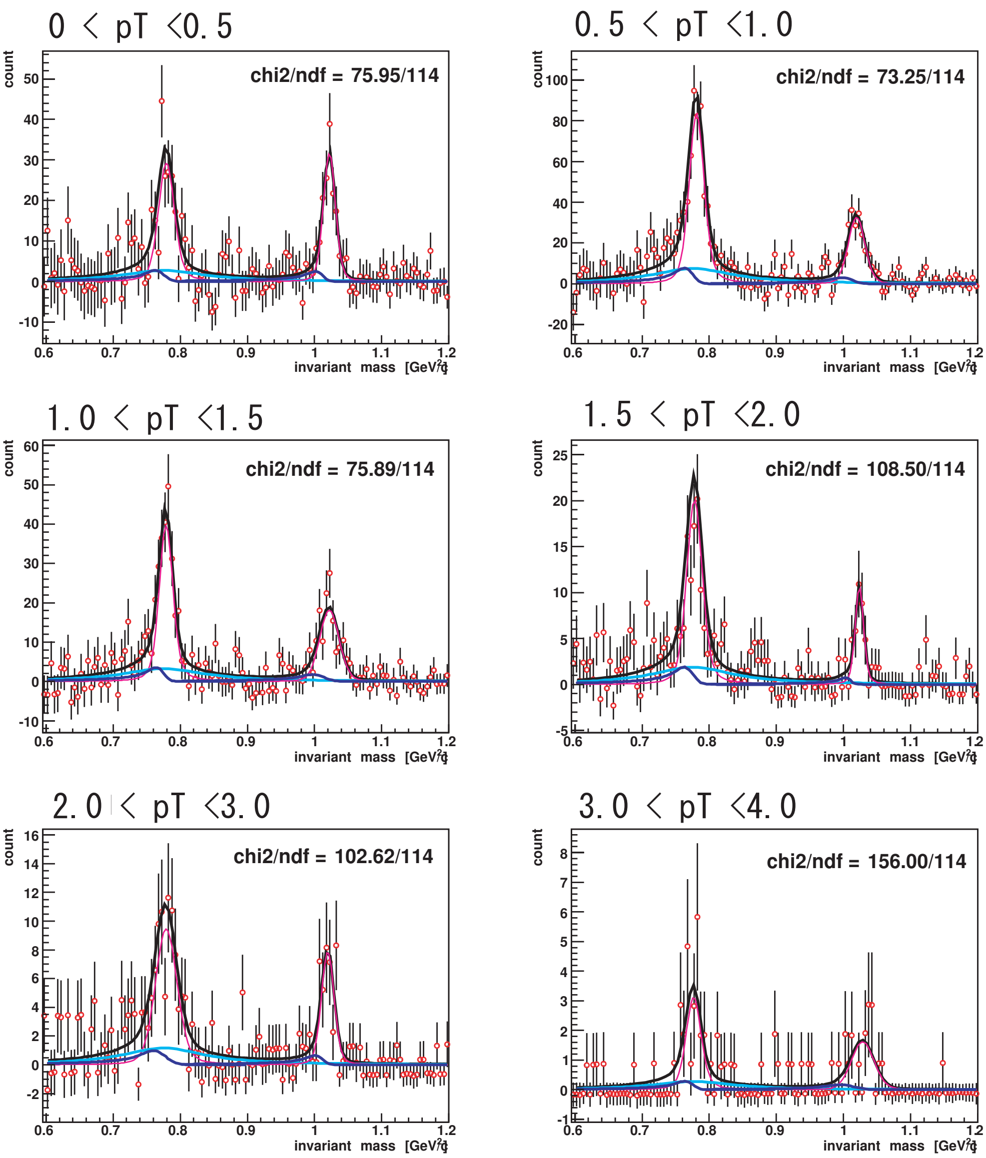

Figure 3.17: Invariant mass spectra divided by pT bins after background subtraction. The black line are the fitting result, which is sum of the known decays, ω (left magenta line), ϕ (right magenta line), ρ (light blue line), radiative decay of ω and ϕ (blue line).

3.5 Efficiency evaluation

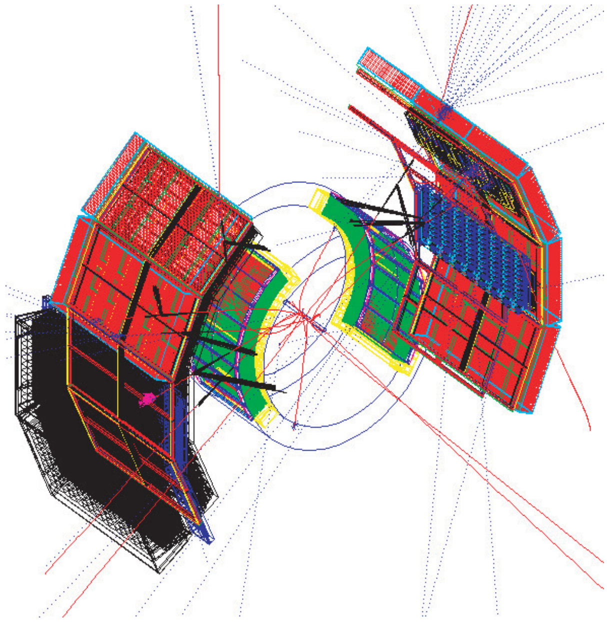

Figure 3.18: Demonstration of tracks decayed from 10 ϕ mesons. The red line indicate e^+ or e^-, blue dotted line indicate photons and black line indicate cherenkov photon radiated in RICH. EMCal, PC and DC are drawn.

To evaluate the efficiency of PHENIX detector acceptance, electron identified and ERT trigger efficiency, the simulation study was done. We use the event generator called "EXODUS" based on Monte Carlo codes. 10M ω mesons and ϕ mesons are generated for following status, and decayed into e^+e^- pair.

- rapidity
  - range: -0.5<y<0.5, the shape of y distribution: flat
- pT (transverse momentum)
  - range: 0.0<pT<5.5, the shape of pT distribution: flat

The PHENIX detector is very complex in character with a large variety of detector types and materials inside it. To simulate such PHENIX detector, "PISA", PHENIX Integrates Simulation Application [32] was introduced. The PISA code is based heavily on the CERN software libraries [33]. Specifically, PISA is the PHENIX implementation of the GEANT geometry and event particle tracking software system. Using PISA, a PHENIX simulator can pick which (or all) aspects of the whole PHENIX detector geometry to introduce into an event simulation. [34]

We reconstruct ω and ϕ mesons by calculating eq. 3.2. The Figure 3.20 is invariant mass spectrum of single ω reconstructed from PISA output.

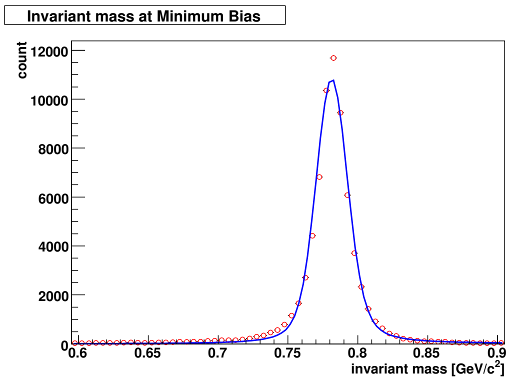

Figure 3.19: Invariant mass spectrum of single ω for all p_T

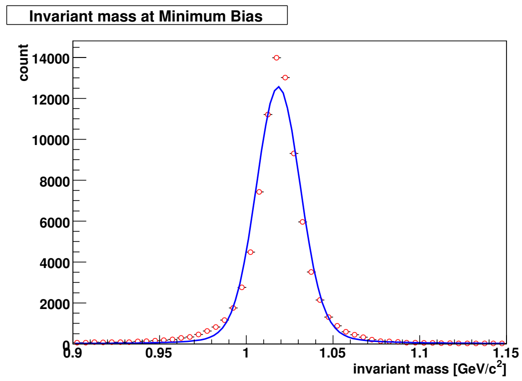

Figure 3.20: Invariant mass spectrum of single ϕ for all p_T

3.5.1 Geometrical Acceptance and Electron ID Efficiency

The efficiency of the PHENIX Geometrical acceptance and electron ID was calculated as a function of pT. Results are shown in Fig.3.22.

In the acceptance calculation, it is important that the detector acceptance in the real data and the simulation data agree. In Fig.3.21, we compare the phi distribution of the data and simulation. Here phi is the ϕ coordinate of track in the DC. The phi distribution in the simulation agree with the real data well.

3.5.2 Trigger efficiency

Single electron efficiency in each EMCal sector for ERT electron is calculated as a function of momentum using Minimum Bias sampled events. The result are shown in Fig.3.23, and called turn-on curve.
Trigger efficiency is calculated with simulation data and turn-on curve. Turn-on curve is fitted by "Error function(Erf)" ,which is integrated gaussian, and

parameterized.

$$f(momentum) = par[0] \times Erf(\frac{momentum - par[2]}{par[1]}) \tag{3.12}$$

A random number is used to see if each electron from the ω and ϕ would have fired Electron trigger in the EMCal sector that it hit, using pT dependent single electron efficiencies shown in Fig.3.23. The results are shown in Fig.3.24.

3.5.3 bin shift correction

Bin shift correction was performed in the same way as used in [38]. The procedure is below.

1. Fit the pT spectrum with f(pT) = exp{-pT/C_1 + C_2 }
2. calculate bin shift correction factor
3. move the data point vertically and leave the pT of data point unchanged.

The result is shown in Table.3.3

pT	0.-0.5	0.5-1.0	1.0-1.5	1.5-2.0	2.0-3.0	3.0-4.0
ω	1.084	1.084	1.084	1.084	1.363	1.363
ϕ	1.065	1.065	1.065	1.065	1.277	1.277

Table 3.3: Correction factor of bin shift correction.

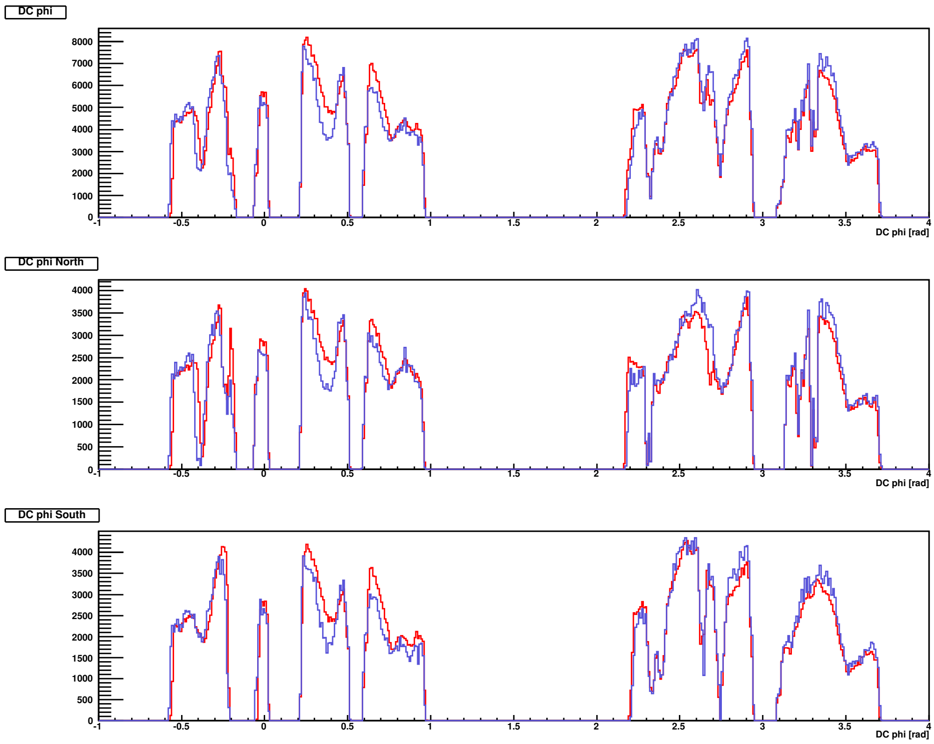

Figure 3.21: Comparison of DC phi distribution in the real data(red) and the simulation(blue). The simulation phi distribution is weighted by appropriate electron p_T distribution. The data is rescaled such that the integral of the phi distribution in the real data and in the simulation agree. The middle and the bottom panel shows the phi distribution in the South side(zed<0)and the North side(zed>0), respectively. The top panel shows the phi distribution for North and South side. The p_T range of the electron is $0.3<p_T<4.0$ GeV/c for borht of the real data and simulation.

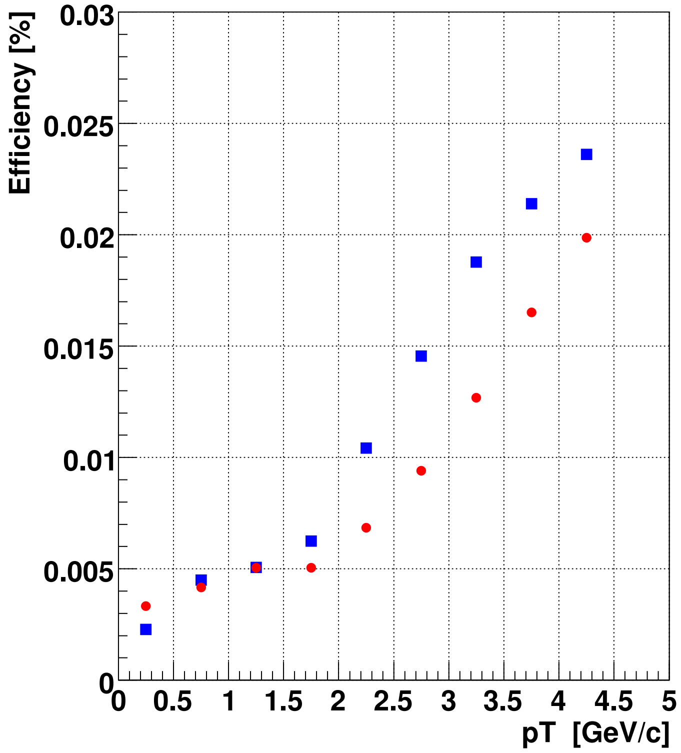

Figure 3.22: Total reconstruction efficiency of ω(blue) and ϕ(red) including acceptance is shown as a function of p_T.

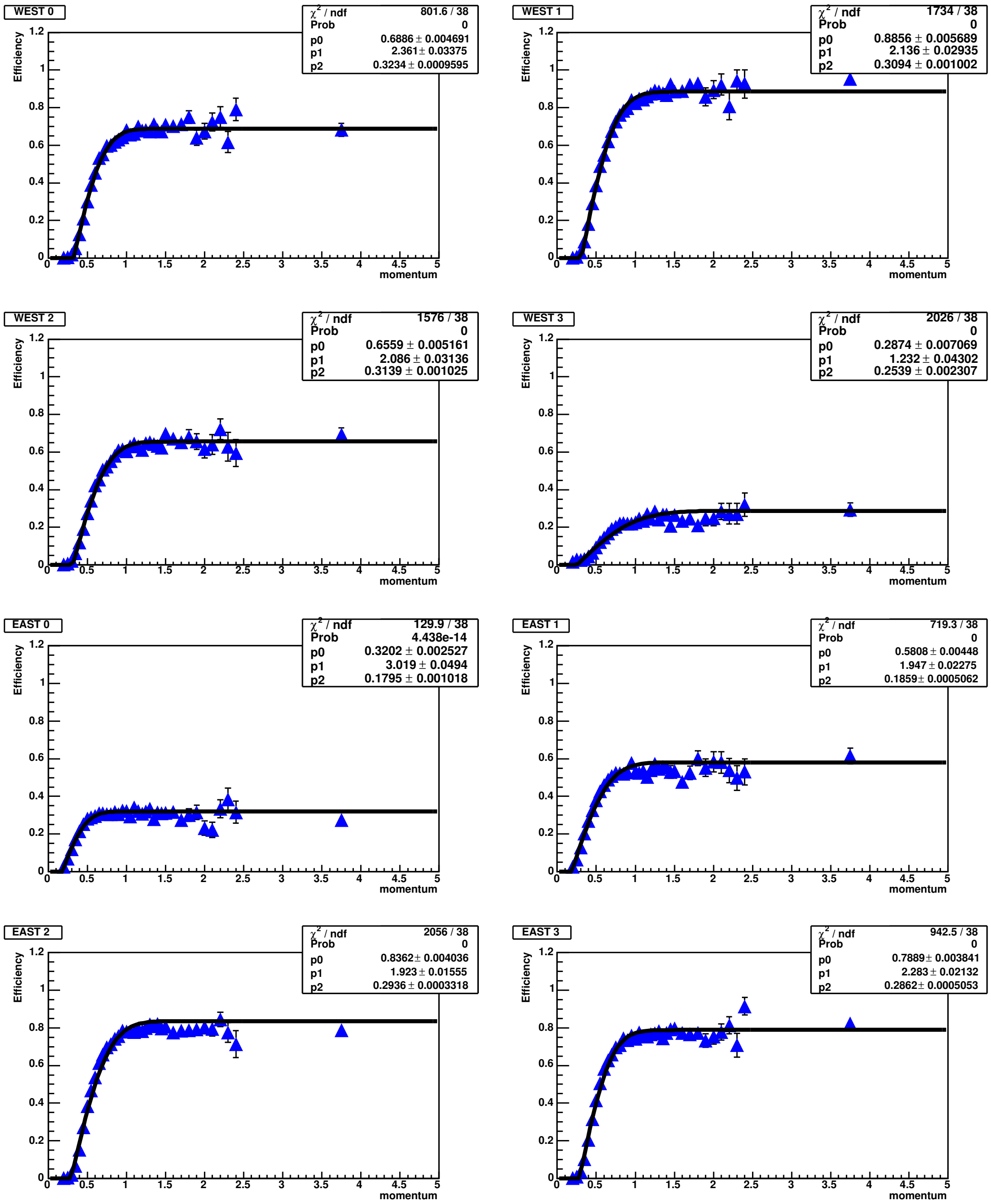

Figure 3.23: ERT Electron trigger efficiency for single electron is shown as a function of momentum.

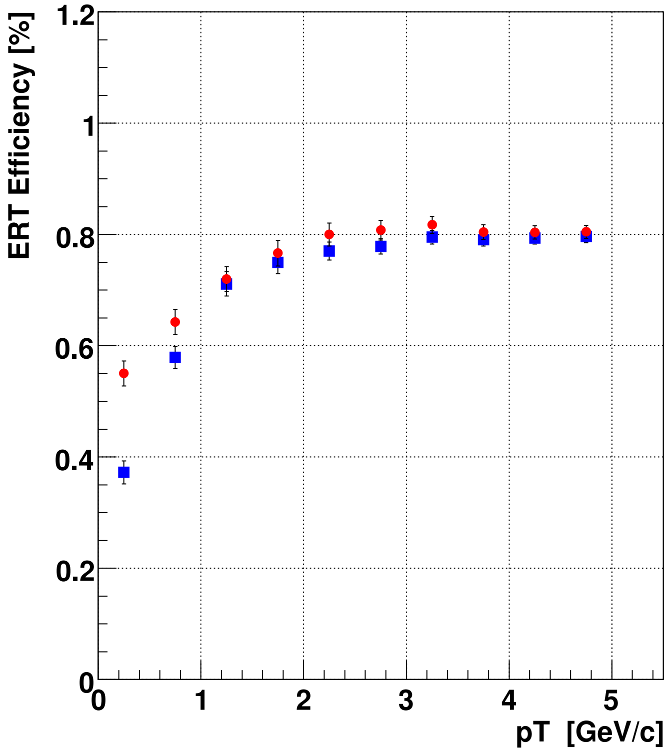

Figure 3.24: ERT Electron trigger efficiency for ω(blue) and ϕ(red) are shown as a function of p_T.

3.6 Systematic Errors

The followings are considered and evaluated as sources of systematic errors.

- signal counting
- geometrical acceptance calculation
- electron ID efficiency
- ERT Trigger efficiency
- Bin shift correction

3.6.1 Signal counting

The source of systematic error in signal counting are following.

- ambiguity of background shape
- ambiguity of rho meson yield

To estimate the systematic error from ambiguity of background, we assumed the other fitting function for background on invariant mass spectra.

$$\begin{aligned} Basic\ method &: Event\ Mixing\ method \\ exponential &: Exp(C_1 \times x\ +\ C_2) \\ power &: C_1 \times Exp(C_2 \times Log(x)\ +\ C_3) \end{aligned}$$

The total systematic error from ambiguity of background was obtained by calculating the quadratic sum of systematic error on the cases of each other fitting function for each p_T bin. The fitting results are shown in Figure 3.25, 3.26. Systematic errors from ambiguity of background for ω and ϕ is shown in Table 3.4, **??**, respectively.

pT	0.-0.5	0.5-1.0	1.0-1.5	1.5-2.0	2.0-3.0	3.0-4.0
pol2	22.6%	0.0%	0.0%	36.5%	15.9%	1.5%
power	16.2%	6.1%	2.4%	34.9%	14.0%	2.4%
total	27.8%	6.1%	2.4%	50.5%	21.2%	2.9%

Table 3.4: Systematic errors from ambiguity of background for ω in each p_T bins .

pT	0.-0.5	0.5-1.0	1.0-1.5	1.5-2.0	2.0-3.0	3.0-4.0
expo	0.7%	8.0%	5.0%	11.5%	2.5%	10.2%
power	2.1%	5.8%	5.2%	10.4%	1.5%	3.9%
total	2.2%	9.8%	7.2%	15.5%	2.9%	10.9%

Table 3.5: Systematic errors from ambiguity of background for ϕ in each p_T bins .

3.6.2 geometrical acceptance calculation

Sources of systematic error in acceptance calculation is difference of fiducial area between the real data and the simulation. The normalization is done in 4 different place as shown Fig.3.27 ,3.28 3.29 ,3.30 to estimate the systematic error from acceptance calculation. the systematic error was estimated by following calculation in each p_T bin.

$$Sys\ Error \ = \ \frac{2 \ \times \ D}{\sqrt{12}} \tag{3.13}$$

D is the deviation which is the ratio between number of ω or ϕ mesons for each case and number of ω or ϕ for basic case.

The deviation is calculate from ratio of integral between the real data and the simulation. The systematic error from acceptance calculation was obtained from Eq.3.13. Then, the D is a largest deviation in all case. The result is shown in Table.3.6.

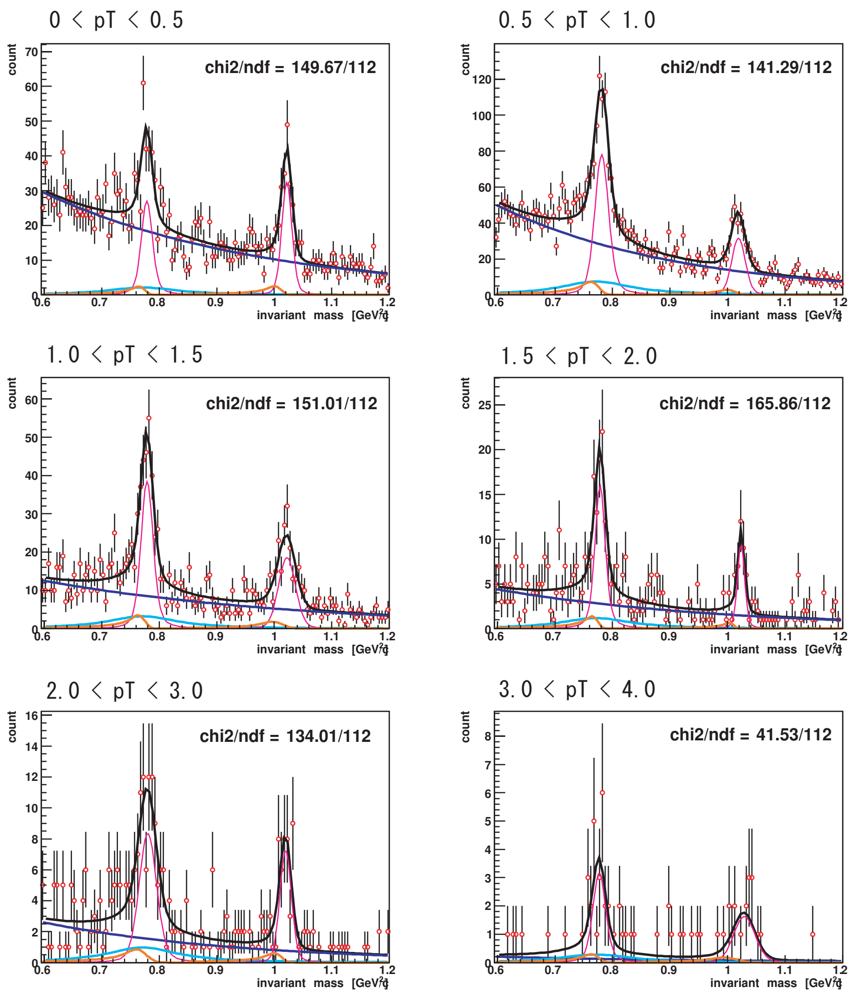

Figure 3.25: Invariant mass spectrum divided by p_T. Background shape was estimated as exponential(blue). The black line are the fitting result, which is sum of the background and known decays, ω (left magenta line), ϕ (right magenta line), ρ (light blue line), radiative decay of ω and ϕ (Orange line)

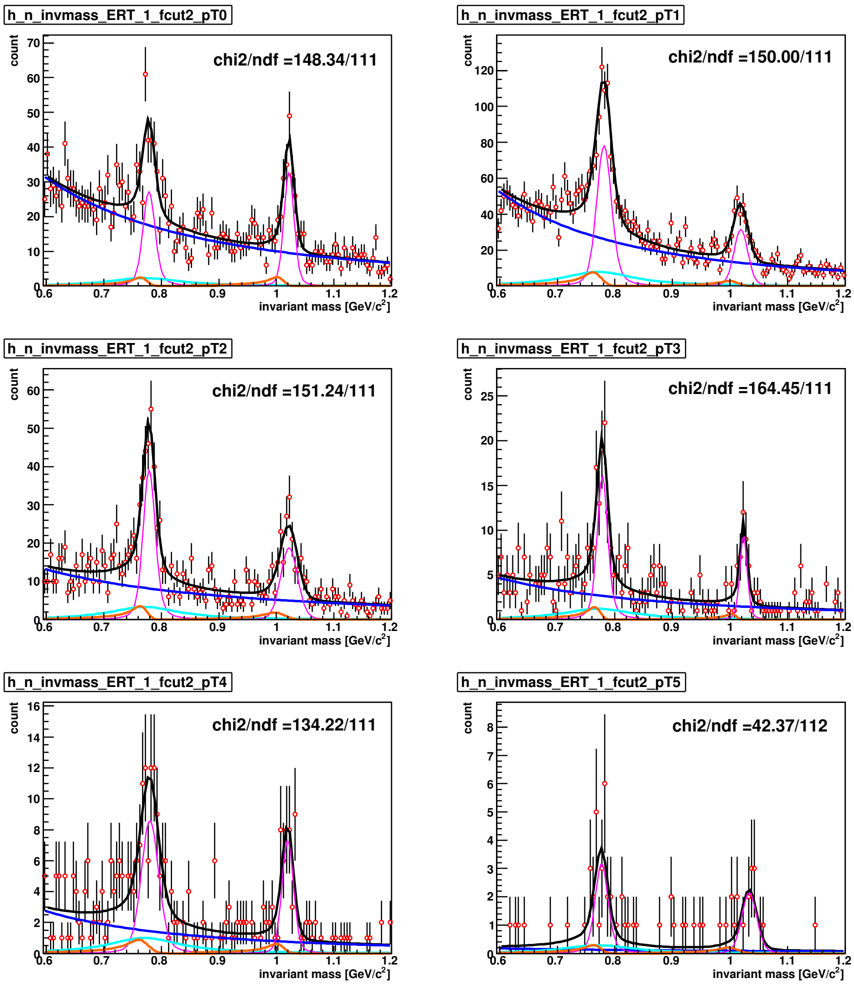

Figure 3.26: Invariant mass spectrum divided by p_T. Background shape was estimated as power law function(blue). The black line are the fitting result, which is sum of the background and known decays, ω (left magenta line), ϕ (right magenta line), ρ (light blue line), radiative decay of ω and ϕ (Orange line)

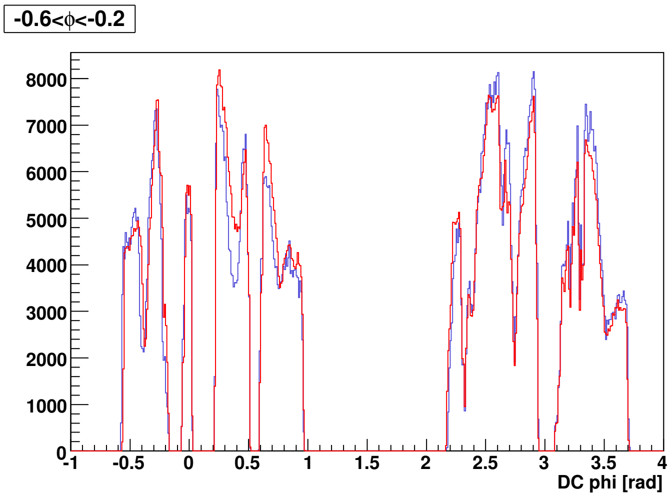

Figure 3.27: phi distribution for the real data(red) and the simulation(blue). Simulation data is normalized in -0.6<ϕ<-0.2

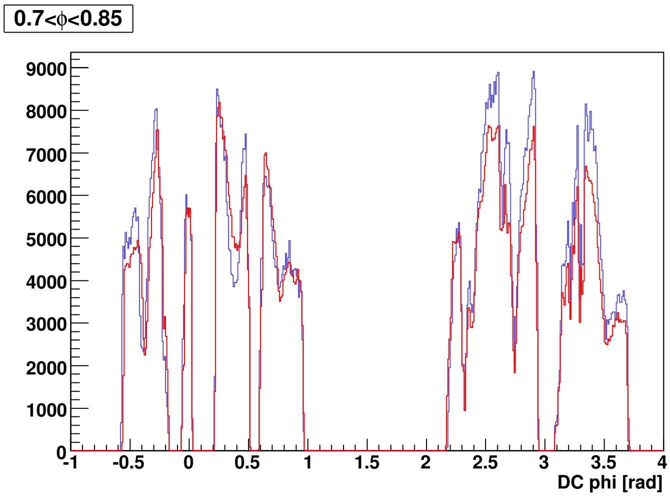

Figure 3.28: phi distribution for the real data(red) and the simulation(blue). Simulation data is normalized in 0.7<ϕ<0.85

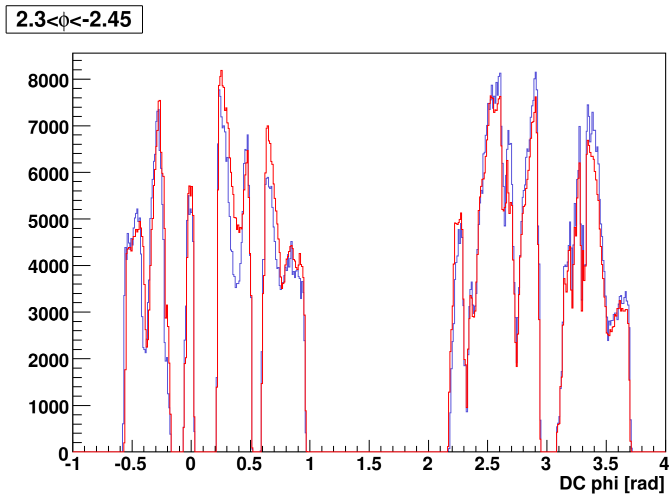

Figure 3.29: phi distribution for the real data(red) and the simulation(blue). Simulation data is normalized in 2.3<ϕ<2.45

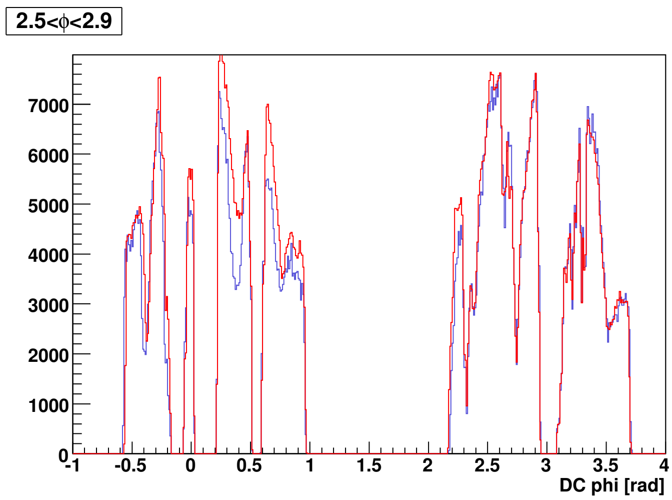

Figure 3.30: phi distribution for the real data(red) and the simulation(blue). Simulation data is normalized in 2.5<ϕ<2.9

ϕ[rad]	-0.6<ϕ<-0.2	0.7<ϕ<0.85	2.3<ϕ<2.45	2.5<ϕ<2.9
deviation	0.945	1.049	1.079	1.011
sys error	4.5%			

Table 3.6: Systematic errors from acceptance calculation.

3.6.3 electron ID efficiency

Systematic error from eID efficiency is assigned to be 8%, since the error assigned in singe electron analysis is 4% [39].

3.6.4 trigger efficiency

To estimate the systematic error from ERT trigger efficiency, parameter of turn-on curve is changed to following.

1. 1.025 $\times$ par[0] and 0.99 $\times$ par[2]

2. 0.975 $\times$ par[0] and 1.01 $\times$ par[2]

Here, par[0] and par[2] are parameter of turn-on curve shown Eq.3.12. the value of 1.025, 0.975, 0.99 and 1.01 were obtained from the error of fitting. Then, case 1 means ERT trigger efficiency is higher than basic. case 2 means ERT trigger efficiency is lower than basic case. For example, the red dash line in Fig.3.31 shows case 1, and the blue dash line shows case 2. After the recalculating trigger efficiency of ω and ϕ, larger $SysError$ calculated by Eq.3.13 in each pT bin was assigned as systematic error. The result is shown in Table.3.7.

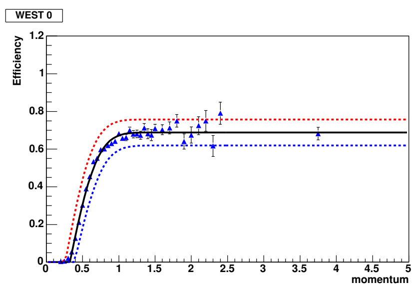

Figure 3.31: single electron ERT trigger efficiency of a sector0. the red dash line shows case1 and the blue dash line shows case2.

pT	0.-0.5	0.5-1.0	1.0-1.5	1.5-2.0	2.0-3.0	3.0-4.0
ω	2.4%	1.8%	1.3%	1.3%	1.1%	1.1%
ϕ	0.8%	2.2%	1.5%	1.1%	1.2%	0.8%

Table 3.7: Systematic errors from ERT trigger efficiency in each p_T bins .

3.6.5 Bin shift correction

Another fitting function:

$$par[0] \times (1 + (\frac{p_T}{par[1]})^2\ )^{-6} \tag{3.14}$$

is bin shift correction is tried for evaluation of systematic error. The difference is assigned as the systematic error from bin shift correction. The result is shown in Table.3.8.

pT	0.-0.5	0.5-1.0	1.0-1.5	1.5-2.0	2.0-3.0	3.0-4.0
ω	11.2%	4.6%	1.1%	3.4%	10.0%	1.0%
ϕ	8.8%	4.3%	3.1%	2.7%	10.5%	4.7%

Table 3.8: Systematic errors from bin shift correction in each p_T bins .

3.6.6 Total systematic error

Various systematic errors are summarized in Table.3.9, 3.10.

pT	0.-0.5	0.5-1.0	1.0-1.5	1.5-2.0	2.0-3.0	3.0-4.0
rho	2.3%					
BG	27.8%	6.1%	2.4%	50.5%	21.2%	2.9%
acceptance	4.5%					
electron ID	8.0%					
ERT trigger	2.4%	1.8%	1.3%	1.3%	1.1%	1.1%
bin shift	11.2%	4.6%	1.1%	3.4%	10.0%	1.0%
Total	31.5%	12.3%	9.9%	51.1%	25.3%	10.0%

Table 3.9: Total systematic error for ω

pT	0.-0.5	0.5-1.0	1.0-1.5	1.5-2.0	2.0-3.0	3.0-4.0
rho	0.6%					
BG	2.2%	9.8%	7.2%	15.5%	2.9%	10.9%
acceptance	4.5%					
electron ID	8.0%					
ERT trigger	0.8%	2.2%	1.5%	1.1%	1.2%	0.8%
bin shift	8.8%	4.3%	3.1%	2.7%	10.5%	4.7%
Total	12.9%	14.3%	12.2%	18.3%	14.3%	15.0%

Table 3.10: Total systematic error for ϕ

Chapter 4

Results and Discussion

4.1 Mass shift

The center of mass was obtained as a function of p_T by fitting the invariant mass spectra for both ω and ϕ, respectively. Figure 4.1 and 4.2 shows the result of the position of mass center as a function of p_T. The obtained results were not consistent with PDG value [29] into the statistical error.

It is necessary to consider the simulation result to evaluate detector mass resolution. The orange line in Figure 4.1 and 4.2 indicate 1σ of detector mass resolution. The position of the mass center obtained by real date are consistent with PDG value, in addition simulated position of mass, within the detector mass resolution.

4.2 Invariant cross section

Invariant cross section in proton+proton collisions for ω and ϕ mesons are calculated as following.

$$E\frac{d^3\sigma}{dp^3} = \frac{1}{2\pi p_T}\frac{N_{\omega\ or\ \phi}}{N_{event}\ \Delta p_T \Delta y}\frac{\sigma_{BBC}}{\epsilon_{bias}}\frac{1}{\epsilon_{acc+eID}\ \epsilon_{ERT}} \tag{4.1}$$

Here

- N_{event} is the Number of MinBias sampled events.
- $\sigma_{BBC} = 23.0$[mb] is the BBC trigger cross section [39].
- $\epsilon_{bias} = 0.79$ is the BBC trigger efficiency [39].
- $\epsilon_{acc+eID}$ is the acceptance and electron reconstruction efficiency.

- ϵ_{ERT} is the ERT trigger efficiency.

After bin shift correction, we were able to get invariant cross section of ω and ϕ mesons as a function of p_T. The Results are shown in Fig.4.5 and 4.6. We compared with results obtained from study of other decay channels, $\omega \rightarrow pi^0\gamma$, $\omega \rightarrow \pi^0\pi^+\pi^-$ and $\phi \rightarrow K^+K^-$ in proton+proton collisions at $\sqrt{s}$ = 200GeV.

The result of this analysis are consistent with the other result within statistical and systematic error.

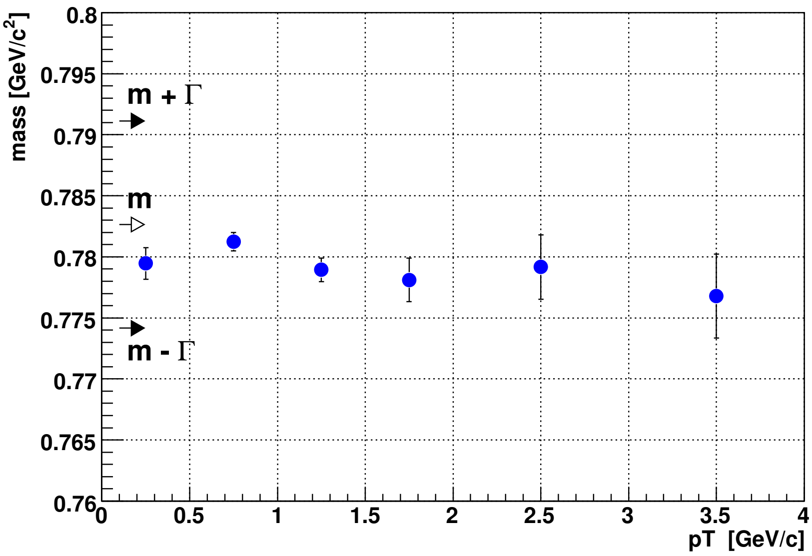

Figure 4.1: position of mass center of ω as a function of p_T. The error is only statistical error. The PDG value [29] of mass center of ω is described in this figure as m, and Γ means total decay width of ω (See table 3.2).

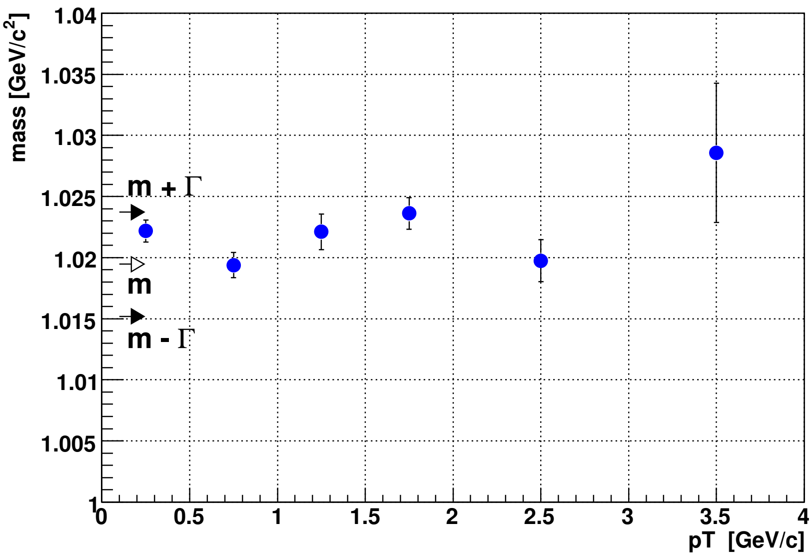

Figure 4.2: mass center of ϕ as a function of p_T. The error is only statistical error. The PDG value [29] of mass center of ϕ is described in this figure as m, and Γ means total decay width of ϕ (See table 3.2).

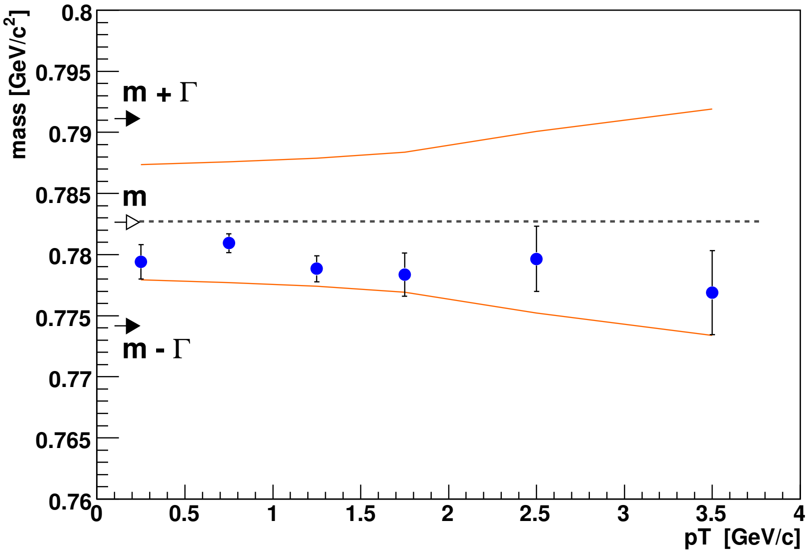

Figure 4.3: mass center of ω as a function of p_T. The blue points are obtained by fitting result for real data analysis. the orange lines indicate 1σ of detector mass resolution obtained by simulation.

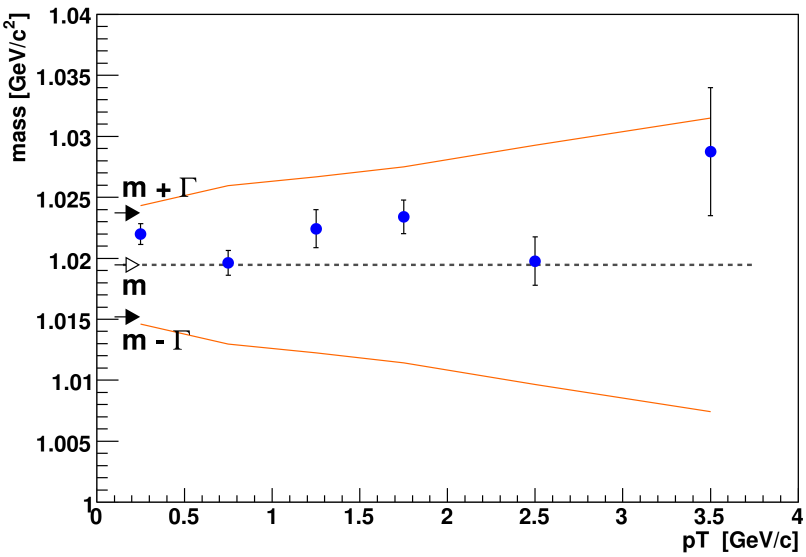

Figure 4.4: mass center of ϕ as a function of p_T. The blue points are obtained by fitting result for real data analysis. the orange lines indicate 1σ of detector mass resolution obtained by simulation.

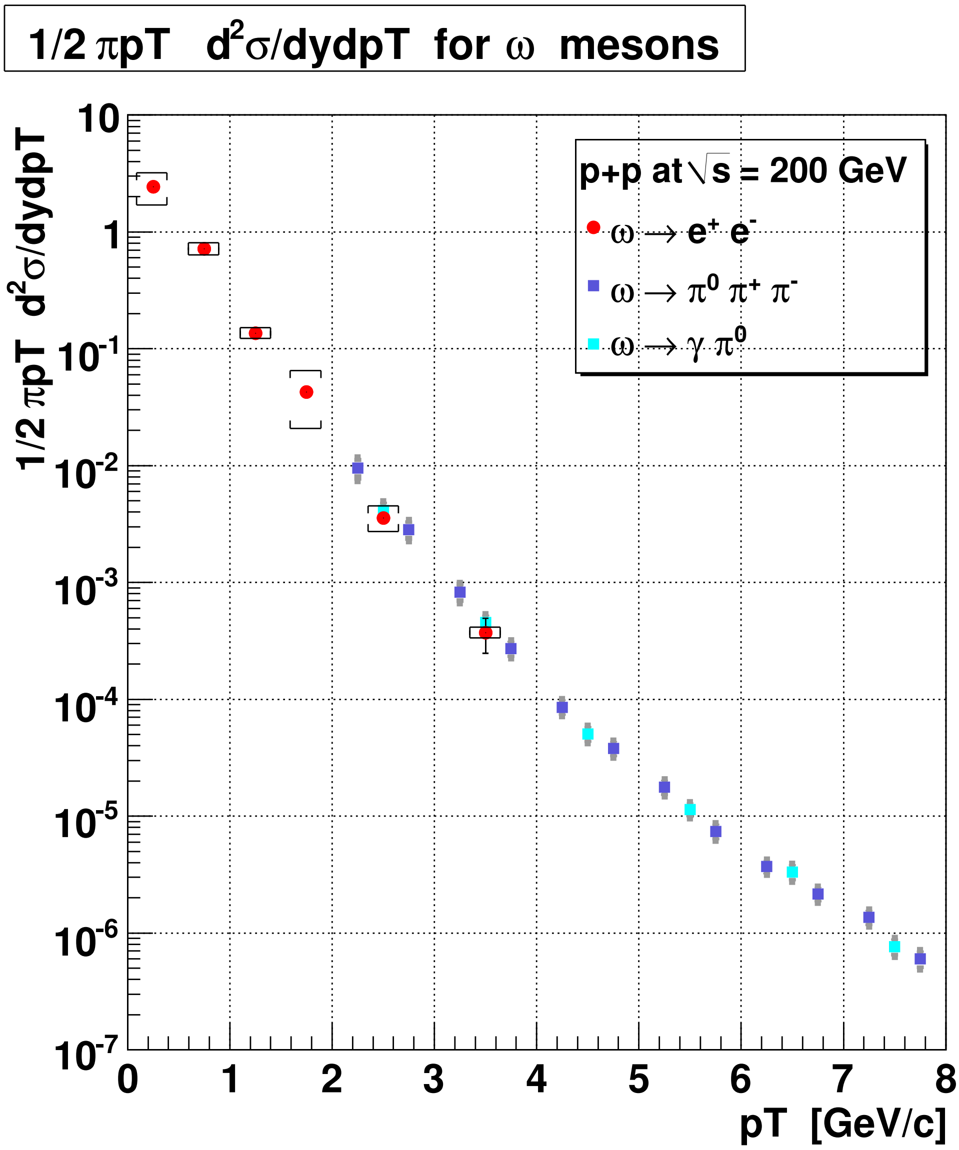

Figure 4.5: Invariant cross section for ω as a function of p_T. The red point is our result, $\omega \to e^+e^-$. The blue and light blue points indicate $\omega \to \pi^0\pi^+\pi^-$, $\omega \to \pi^0\gamma$, respectively. The bracket and gray band indicate systematic error.

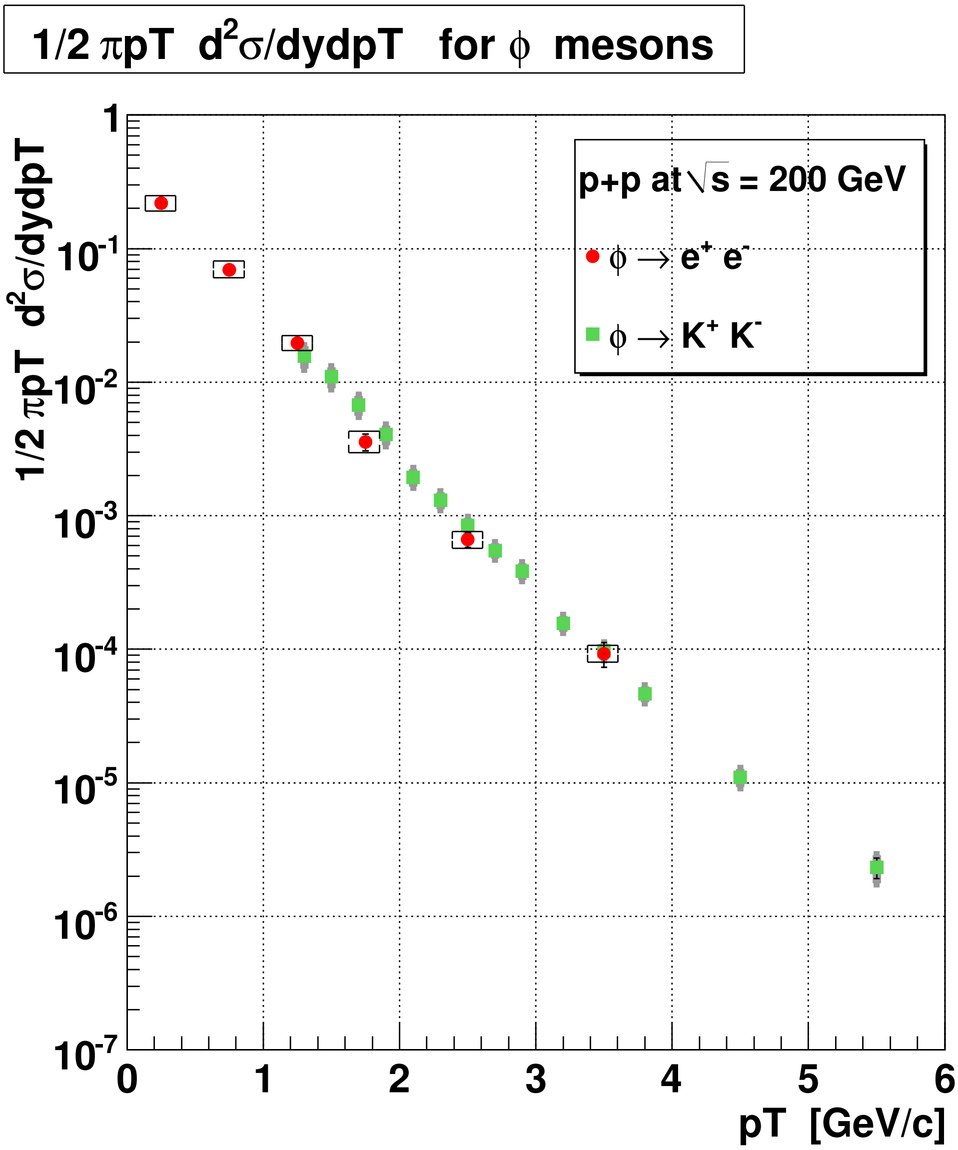

Figure 4.6: Invariant cross section for ϕ as a function of p_T. The red point is our result, $\phi \to e^+e^-$. The green points indicate $\phi \to K^+K^-$. The bracket and gray band indicate systematic error.

Chapter 5

Conclusion

We have measured the invariant mass spectra of e^+e^- pairs and obtained production cross section as a function of p_T in proton+proton collisions at $sqrts = 200$GeV. The goal of this work is to find out whether mass shift and modification of the light vector mesons are detected or not, in proton+proton collisions and to provide reference data as baseline of heavy ion collision.

We identified e^+, e^- tracks from large other charged particle tracks produced in the collision vertex. We reconstructed the invariant mass spectrum of e^+e^- pairs and subtracted combinatorial background evaluated by event mixing method, moreover fitted the resonance function as known source, $\omega \to e^+e^-$, $\phi \to e^+e^-$, $\rho \to e^+e^-$ and radiative tail.

We observed no mass shift in proton+proton collisions. The position of center of mass are consistent with PDG value within the detector mass resolution obtained by simulation based on Monte Carlo codes. In addition, the invariant cross section of ω and ϕ mesons are obtained by correcting the acceptance of PHENIX detector, electron identified efficiency, and ERT trigger efficiency. As a consequence of comparison with the result of other decay channels, we recognized that there is no difference.

From this view point, we can provide reference data of ω and ϕ production as baseline of heavy ion collision. The next step, we will be going on the data analysis of heavy ion collisions, Au+Au and Cu+Cu. There is possibility of observation of mass shift and mass modification in heavy ion collision. We will present this results as soon as possible!!

Acknowledgements

I would like to thank the staff members Sugiate-sensi, Homma-sensei, Torii-san, Horaguchi-san and Shigaki-sensei for their detailed comments, suggestions, and constant support. I could not write up this paper without your help. I also would like to thank Ozawa-sensei.

I wish to thank Tsuchimoto-san for giving me very useful advice to proceed my analysis. I also wish to thank Nakamiya-san for discussing with me about useful physics topics at any time day or night. I would like to thanks Narita-kun and Kubo-san for their encouragement. I great acknowledge all members of our lab and H/L PWG.

Finally, thanks appreciate my friends, huyc 14 members, my brother and my mother.

Bibliography

[1] K.Yagi, T.Hatuda and Y.Miake Quark-Gluon Plasma

[2] Phovh.Rith.Scholz.Zetsche, PARTICLES AND NUCLEI

[3] John B. Kogut. *et al*. Phys.Rev.Lett. **50**(1983) 393

[4] M.Lutz, S.Klimt and W.Weise. Nuclear Physics A **542**(1992) 521-558

[5] G.E.Brown, Mannque Rho. Phys.Rev.Lett. **66**(1991) 2720-2723

[6] K.Yagi, T.Hatuda, H.Shiomi and H.Kuwabara. Prog.Theor.Phys. **95**(1996) 1009-1028

[7] T.Hatsuda and T.Kunihiro. Phys.Rept. **247**(1994) 2221-367. hep-ph/9504250

[8] G.Agakichiev, *et al*, Nuclear Instruments and Methods A **371**(1996) 16-21

[9] CERES Collaboration, D.Adamova. *et al*. nucl-ex/0611022

[10] NA60 Collaboration, R.Arnaldi. *et al*. Phys.Rev.Lett. **96**(2006) 162302

[11] M.Sekimoto, *et al*, Nuclear Instruments and Methods A **516**(2004) 390-405

[12] KEK-E325 Collaboration, R.Muto. *et al*, Phys.Rev.Lett. **98**(2007) 042501

[13] M.Naruki, *et al*, Phys.Rev.Lett. **96**(2006) 092301

[14] Nuclear Instruments and Methods A **499**(2003) 235-244

[15] Nuclear Instruments and Methods A **499**(2003) 423-432

[16] Nuclear Instruments and Methods A **499**(2003) 549-559

[17] T.Nakamura http://www.phenix.bnl.gov/WWW/run/03/focus/talks/bbc/focus bbc.ppt

[18] Nuclear Instruments and Methods A **499**(2003) 433-436

[19] Nuclear Instruments and Methods A **499**(2003) 480-488

[20] Nuclear Instruments and Methods A **499**(2003) 489-507

[21] Nuclear Instruments and Methods A **499**(2003) 508-520

[22] Nuclear Instruments and Methods A **433**(1999) 143-148

[23] Nuclear Instruments and Methods A **499**(2003) 521-536

[24] Nuclear Instruments and Methods A **499**(2003) 537-548

[25] Nuclear Instruments and Methods A **499**(2003) 560-592

[26] Nuclear Instruments and Methods A **499**(2003) 593-602

[27] in PHENIX website http://www.phenix.bnl.gov/WWW/run/drawing/

[28] M.Naruki. PhD thesis, Kyoto Univ., 2006

[29] K.Hagiwara, *et al.* Review of Particle Physics. *Phys.Rev.D*, 66:010001, 2002.

[30] Fermilab E760 Collaboration, T.A.Armstrong, *et al.* Phys.Rev.D **54**(1996) 7067-7070

[31] A.Spiridonov hep-ex/ **0510076**

[32] A Primer Manual for the PHENIX Simulation Code PISA http://www.phenix.bnl.gov/phenix/WWW/simulation/primer4/

[33] CERN Official Website, http://www.cern.ch

[34] M.Ouchida. Master thesis, Hiroshima Univ., 2007

[35] $quality\ control\ for\ RUN5\ pp\ data\ set$. PHENIX analysis note 486

[36] PHENIX analysis note 550

[37] PHENIX analysis note 411

[38] PHENIX analysis note 73

[39] $Single\ electrons\ from\ heavy-flavor\ decays\ in\ p+p\ collisions\ at\ \sqrt{s}=200GeV$. PHENIX analysis note 509